



The IFIT2–IFIT3 antiviral complex targets short 5' untranslated regions on viral mRNAs for translation inhibition

Received: 17 January 2025

Accepted: 2 September 2025

Published online: 15 October 2025

Check for updates

Dustin R. Glasner¹, Candace Todd¹, Brian Cook², Agustina D’Urso¹,
Shivani Khosla¹, Elena Estrada¹, Jaxon D. Wagner¹, Mason D. Bartels^{3,4},
Chuan-Tien Hung⁵, Pierce Ford¹, Jordan Prych¹, Kathryn S. Hatch¹,
Brian A. Yee^{6,7,8}, Kaori M. Ego⁶, Qishan Liang⁶, Sarah R. Holland¹,
James Brett Case¹, Kevin D. Corbett^{1,6}, Michael S. Diamond^{9,10,11},
Benhur Lee¹⁰, Gene W. Yeo^{6,7,8,12}, Mark A. Herzik Jr², Eric L. Van Nostrand^{3,4} &
Matthew D. Daugherty¹✉

Recognition of foreign RNA is critical for the innate immune response to viruses. Interferon (IFN)-induced proteins with tetratricopeptide repeats (IFIT) 2 and 3 are highly upregulated following viral infection, but mechanistic insight into their antiviral role is lacking. Here we demonstrate that short 5' untranslated regions (UTRs), a characteristic of many viral mRNAs, can serve as a molecular pattern for innate immune recognition via IFIT2 and IFIT3. Structure determination of the IFIT2–IFIT3 complex at 3.2 Å using cryo-EM reveals a domain-swapped heterodimer that is required for recognition of the viral mRNA 5' end, translation inhibition and antiviral activity. Critically, viral or host 5' UTR lengths less than 50 nucleotides are necessary and sufficient to enable translation inhibition by the IFIT2–IFIT3 complex. Accordingly, diverse viruses whose mRNAs contain short 5' UTRs, such as vesicular stomatitis virus and parainfluenza virus 3, are sensitive to IFIT2–IFIT3-mediated antiviral activity. Our work thus reveals a pattern of antiviral nucleic acid immune recognition that takes advantage of the inherent constraints on viral genome size.

Recognition of foreign RNA is a critical component of immune sensing during viral infection. Interferon (IFN) serves as the first line of defence against viral infection, and its induction is triggered by one of several mechanisms sensing ‘non-self’ RNA or DNA in host cells. IFN signalling induces expression of a number of proteins (for example, OAS, MDA5 and PKR), which themselves bind to double-stranded RNA (dsRNA) in the cytoplasm to amplify innate immune signalling and activation, promote RNA degradation, or inhibit messenger (m)RNA translation^{1–5}. Analogously, dsDNA sensing in the cytoplasm by cGAS and other proteins is essential for activation of IFN responses^{6–8}. Other RNAs can be recognized as foreign, including RNAs with an uncapped 5'

tri- or di-phosphate end by RIG-I^{1,2,5}, mRNAs with high CG-dinucleotide content by zinc finger antiviral protein (ZAP/PARP13)⁹, and endosomal single-stranded RNA (ssRNA) by TLR7 and TLR8 (ref. 10). Notably, some of these patterns are also found on ‘self’ nucleic acids, including dsDNA and CG-dinucleotides. Despite this, these nucleic acid sensing proteins comprise a multifaceted barrier to infection by a wide range of viruses.

Among the many RNA-sensing innate immune proteins are the IFIT (IFN-induced proteins with tetratricopeptide repeats) proteins, coded by an evolutionarily dynamic family of genes that is highly upregulated during viral infection^{11–13}. Notably, IFIT1 and IFIT1B proteins recognize ‘non-self’ methylation patterns on the 5' cap structures of viral mRNAs,

A full list of affiliations appears at the end of the paper. ✉ e-mail: mddaugherty@ucsd.edu

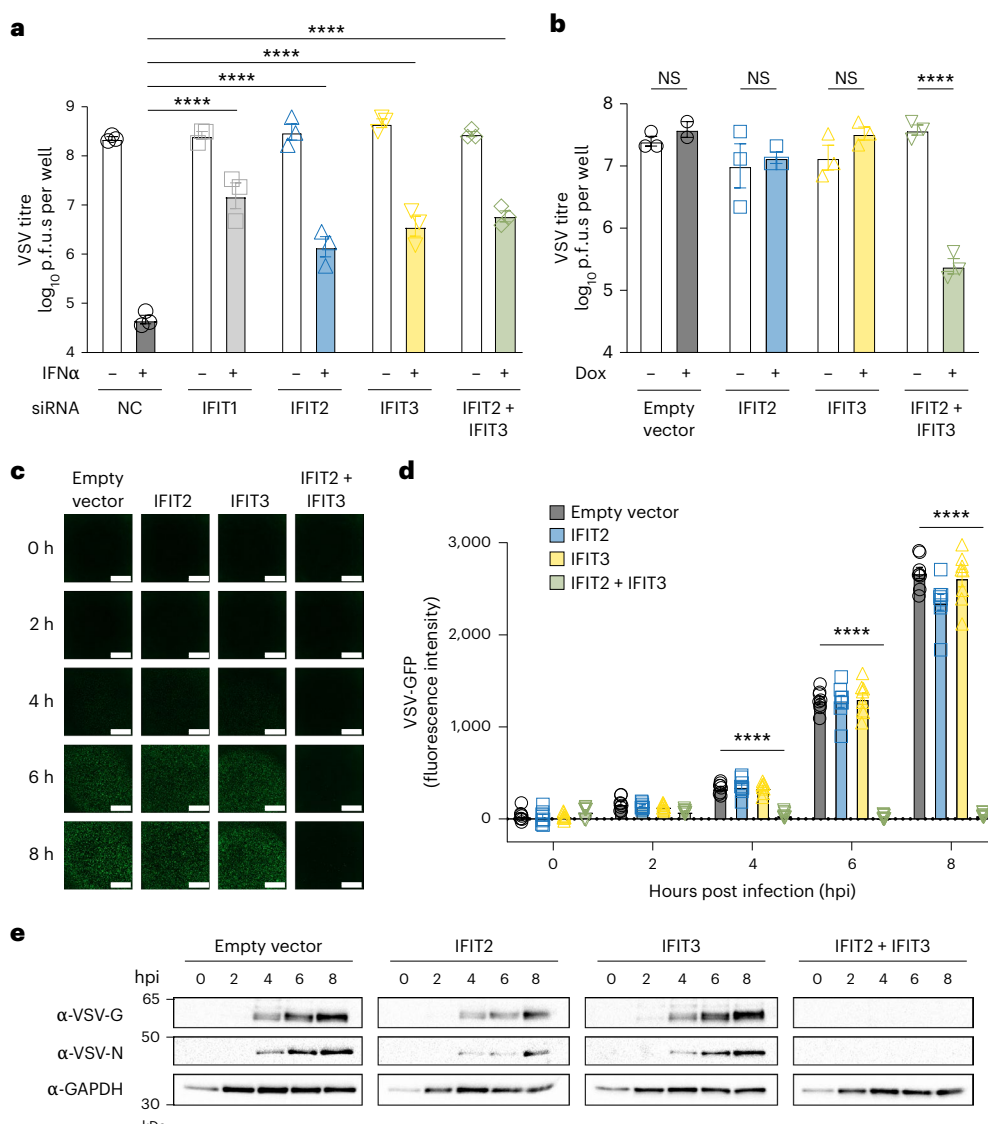


Fig. 1 | IFIT2 and IFIT3 act together to inhibit viral replication. **a**, Human A549 cells were treated with a non-targeting control siRNA (NC, black circles) as a negative control, or siRNA targeting IFIT1 (light grey squares), IFIT2 (blue triangles), IFIT3 (yellow triangles), or IFIT2 and IFIT3 in combination (green diamonds). In indicated conditions, cells were induced with IFN α (1,000 U ml $^{-1}$). All cells were infected with VSV-GFP (0.01 MOI), and supernatant was collected at 16 hpi for titration ($n = 3$ biological replicates). p.f.u.s, plaque-forming units. **b**, Inducible Flp-In T-REx HEK293 cells expressing no IFIT (black circles), mouse IFIT2 (blue squares), mouse IFIT3 (yellow triangles), or mouse IFIT2 and IFIT3 together (green triangles) were mock treated or treated with doxycycline (500 ng μ l $^{-1}$) for 24 h and then infected with VSV-GFP (0.01 MOI). Supernatant was collected at 24 hpi for titration ($n = 3$ biological replicates). **c–e**, Using the same

cell lines as in Fig. 1b, each cell line was treated with doxycycline (500 ng μ l $^{-1}$) for 24 h and infected with VSV-GFP (3.0 MOI). **c**, Images were taken at 0, 2, 4, 6 and 8 hpi. Scale bar, 1,000 μ m. **d**, Images from experiments shown in c were processed and quantified for GFP fluorescence intensity ($n = 8$ biological replicates).

e, Lysates from infected cells were collected at 0, 2, 4, 6 and 8 hpi and analysed by western blotting for expression of two viral proteins, VSV-G and VSV-N, and a loading control, GAPDH. All experiments were performed with 3 or more biological replicates with individual datapoints shown (a,b,d) or representative images shown (c). Data are represented as mean \pm s.e.m. Statistical analyses: ordinary two-way analysis of variance (ANOVA) with Tukey's post test and a single pooled variance (a,d); *** $P < 0.0001$; NS, not significant; ordinary two-way ANOVA with Šidák's post test and a single pooled variance (b); *** $P < 0.0001$.

leading to inhibition of their translation^{13–20}. In contrast, the role of IFIT2 and IFIT3 in the antiviral response is less clear. Several studies have implicated IFIT2 and IFIT3 in the restriction of viral infection in vitro and in vivo^{11,21–25}, and human IFIT3 interacts with and potentiates the effects of human IFIT1 (ref. 26). In other studies, IFIT2 has been shown to have a proviral effect on influenza virus replication²⁷ and activate apoptosis^{28–30}, whereas IFIT3 may abrogate IFIT2-induced apoptosis^{28,31}. While these studies indicate that IFIT2 and IFIT3 have important roles in innate immunity, the manner in which IFIT2 and IFIT3 exert direct antiviral effects has remained unclear.

In this study, we demonstrate that IFIT2 and IFIT3 are necessary and sufficient for antiviral activity against vesicular stomatitis virus

(VSV) and parainfluenza virus 3 (PIV3). Using cryo-electron microscopy (cryo-EM), virological experiments and mRNA translation reporter assays, we demonstrate that IFIT2 and IFIT3 form a stable heterodimeric complex that facilitates recognition and translation inhibition of mRNA from several viruses. We determine that the molecular pattern that leads to IFIT2–IFIT3-mediated inhibition is the presence of short (<50 nucleotide (nt)) 5' untranslated regions (5' UTRs), which is a feature of mRNAs from many viral families. Our data elucidate a previously undescribed antiviral role for IFIT2 and IFIT3, and reveal that 5' UTR length is a marker for non-self recognition of viral mRNAs during the innate immune antiviral response.

Results

IFIT2 and IFIT3 combine to exert potent antiviral effects *in vitro*

Studies with knockout mice have shown that IFIT2 and/or IFIT3 are required for antiviral activity against several RNA viruses, including VSV^{11,22–25,32}. We first determined whether IFIT2 and IFIT3 contribute to the antiviral effects of type I IFN against VSV in human cells. Knockdown of either *Ifit1* (as a positive control^{13,14,20}), *Ifit2*, or *Ifit3* in human A549 cells partially rescued viral replication following IFN α treatment (Fig. 1a and Extended Data Fig. 1a–c), suggesting that all three IFITs contribute to the antiviral effect of type I IFN.

Human IFIT1, IFIT2 and IFIT3 can interact with and regulate one another^{14,26,33–35}, making it unclear from the above experiments whether IFIT2 and IFIT3 have antiviral activity distinct from IFIT1. We therefore took advantage of the observation that mouse IFIT3, unlike human IFIT3, does not interact with human IFIT1 (ref. 26) and generated HEK293 cell lines that express mouse IFIT2 and mouse IFIT3 alone or in combination under the inducible control of doxycycline (DOX) (Extended Data Fig. 1d). We confirmed that co-expression of mouse IFIT2 and IFIT3 do not immunoprecipitate human IFIT1, whereas co-expressed human IFIT2 and IFIT3 do (Extended Data Fig. 1e). Upon DOX induction, we observed no decrease in VSV titres when mouse IFIT2 or IFIT3 was expressed alone (Fig. 1b). However, when mouse IFIT2 and IFIT3 were co-expressed in HEK293 cells, we observed a >100-fold decrease in VSV titres (Fig. 1b), which was unchanged when we knocked down human IFIT1 (Extended Data Fig. 1f). Notably, a significant difference in GFP expression from the viral genome can be observed as early as 4 h post infection (hpi) (Fig. 1c,d). Together with our knockdown data, these results indicate that IFIT2 and IFIT3 are both necessary for effective IFN-mediated antiviral activity against VSV and sufficient to attenuate VSV replication when expressed in the absence of IFN stimulation.

We next evaluated the effect of mouse IFIT2 and IFIT3 expression on VSV-encoded protein levels during infection. At 0, 2, 4, 6 and 8 hpi, infected cells were collected and analysed by western blotting. Expression of IFIT2 and IFIT3 together, but not alone, prevented detectable accumulation of VSV-G and -N proteins compared to control cells (Fig. 1e). These data support a model in which IFIT2 and IFIT3 cooperate during the antiviral response to disrupt an early step of viral infection, resulting in lower viral protein expression.

Structure of the mouse IFIT2–IFIT3 heterodimer reveals the basis for antiviral complex assembly

Although IFIT2 and IFIT3 are known to form a stable heterodimer³³, the structural basis of IFIT2–IFIT3 complex formation had not been characterized. We therefore determined the structure of a 1:1 complex of mouse IFIT2 and IFIT3 to 3.2 Å resolution by cryo-EM (Supplementary Table 1 and Extended Data Fig. 2). IFIT proteins are composed of tandem α -helical tetratricopeptide repeats (TPR) that can fold into superhelical spiral structures^{12,15,18,26,36,37}. In the case of monomeric IFIT1 and monomeric IFIT5, the superhelical structure is broken into four domains termed subdomain (SD) I, SD II, Pivot and SD III^{15,18,26}. In our structure, each monomer of the mouse IFIT2–IFIT3 heterodimer also adopts an all- α -helical structure, with IFIT2 containing 22 α -helices and IFIT3 containing 19 α -helices (Fig. 2a–c and Extended Data Fig. 3a–c). In the assembled IFIT2–IFIT3 heterodimer, the two proteins are oriented parallel to one another and associate through a domain swap involving α -helices 7–9 in SD II (Fig. 2b–d and Extended Data Fig. 3a–c). The large, buried surface area that results from this domain swap (>4,000 Å² per protomer) provides a molecular explanation for the stability of the IFIT2–IFIT3 complex³³ and is similar to the domain-swapped topology of a previously published crystal structure of an IFIT2 homodimer³⁷. Importantly, these changes in SD II orientation between IFIT1 and IFIT2–IFIT3 also alter the IFIT association with RNA. In RNA-bound IFIT1 (refs. 15,18,26), α -helices 7–9 in SD II

form a clamp around the bound 5' end of the mRNA, whereas in IFIT2–IFIT3, α -helices 7–9 are domain swapped, such that the equivalent deep clefts in this complex include structural elements from both IFIT2 and IFIT3 (Fig. 2d,e and Extended Data Fig. 3d–f). As a consequence, SD II is shorter in IFIT2 and IFIT3 relative to IFIT1 and IFIT5, and the α -helices C-terminal to SD II (α -helices 10–22 in IFIT2 and α -helices 10–19 in IFIT3) form a single continuous superhelix that comprises SD III (Fig. 2c,d and Extended Data Fig. 3c–f).

To investigate the importance of the domain-swapped SD II, we performed evolutionary analyses on IFIT2 and IFIT3 across species. Consistent with the importance of SD II for function, we observed strong signatures of conservation (purifying selection) for many residues in this region of the protein in both rodents and primates (Fig. 2f, Extended Data Table 1 and Supplementary Table 2). These evolutionary analyses also revealed strong signatures of positive selection acting on several residues in SD I and especially SD III of both IFIT2 and IFIT3 in rodents and primates (Fig. 2f, Extended Data Table 1 and Supplementary Table 2). Such signatures of recurrent positive selection are characteristic of host immunity proteins that are engaged in direct evolutionary arms races with viral antagonists^{38–41}, and similarly strong signatures of positive selection have recently been described for IFIT1 (ref. 20). Our evolutionary analyses thus reveal not only the strong conservation of SD II, but also suggest that IFIT2 and IFIT3 are engaged in host–virus arms races as a result of their antiviral activities.

We next evaluated whether mutations at the heterodimer interface in SD II and the predicted RNA-binding surfaces in SD III would alter antiviral function. At the core of the SD II domain swap in the IFIT2–IFIT3 heterodimer is a pair of reciprocal glutamic acid–lysine (E–K) salt bridges that we hypothesized are important for complex formation and antiviral activity (Fig. 3a). As expected from introduction of a predicted K-to-K charge clash at the core of the heterodimeric interface, co-transfection of IFIT2 and IFIT3 single mutant (E→K) constructs showed reduced antiviral activity against VSV-GFP compared with WT IFIT2 and IFIT3 (Fig. 3b). Importantly, when we reestablished the predicted salt bridges by introducing a second set of K→E mutations, we restored the antiviral activity of IFIT2–IFIT3 (Fig. 3b). We also mutated a well-conserved set of residues in SD III on the basis of previously described mutations that were shown to disrupt mouse IFIT2 and human IFIT3 RNA binding^{37,42} (Fig. 3c). When cells were transfected with these mutant proteins and infected with VSV, we observed a dramatic reduction in antiviral activity relative to transfection with WT IFIT2–IFIT3 (Fig. 3d). These structural and functional data describe the basis for IFIT2–IFIT3 complex formation and its importance for antiviral activity.

The IFIT2–IFIT3 antiviral complex binds VSV mRNAs near the start codons

Several IFITs have been described as having RNA-binding capabilities^{13,18,19,33}. Accordingly, we assessed whether IFIT2 or IFIT3, alone or in combination, interacted with specific regions of VSVRNAs by performing enhanced UV-crosslinking and immunoprecipitation (eCLIP) on cells expressing mouse IFIT2 and/or IFIT3 and infected with VSV.

We first performed experiments in HEK293 cells ectopically expressing mouse IFIT2 and/or IFIT3. When IFIT2 and IFIT3 were expressed together, we observed strong immunoprecipitation of RNA sequences near the 5' end of the positive (protein-coding) strand of each VSV gene and a clear enrichment of viral mRNAs in the eCLIP dataset relative to total RNA (Fig. 4a and Extended Data Fig. 4a,b). The profile of enriched viral RNA was nearly identical for IFIT2 and IFIT3 when co-expressed, whereas we did not observe such enrichment when IFIT2 or IFIT3 was expressed alone. Moreover, we observed the strongest enrichment of sequences crosslinking to IFIT2 and IFIT3 in regions that overlap the 5' UTR and start codons of the VSV mRNA transcripts (Fig. 4a,b). These data suggest that the IFIT2–IFIT3 heterodimer selectively associates with VSV transcripts at sequences proximal to the start codons.

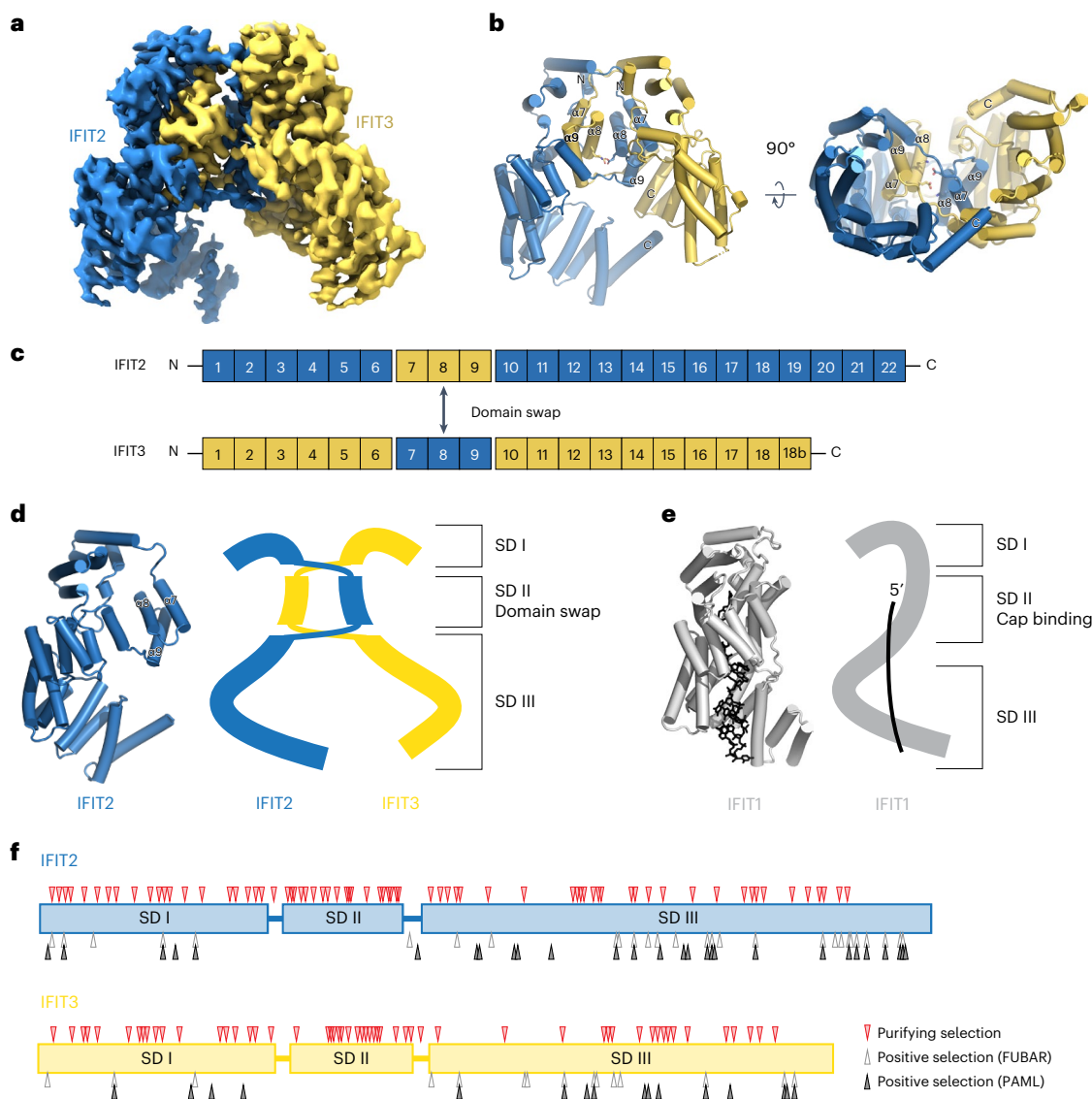


Fig. 2 | Structure of the IFIT2–IFIT3 heterodimer reveals a conserved interaction surface required for antiviral activity. **a**, Cryo-EM density map of the mouse IFIT2–IFIT3 heterodimer. **b**, Structural model of the IFIT2–IFIT3 heterodimer. **c**, Linear model of the IFIT2–IFIT3 heterodimer, with helices indicated, including helices 7–9 that are involved in the domain swap. **d**, Isolated IFIT2 monomer from the structure (left) and schematic of the IFIT2–IFIT3 heterodimer (right), with subdomains (SDs) indicated. The SD

II domain swap, which forms a continuous superhelix with SD I and SD III, is illustrated. **e**, Structure (left) and cartoon (right) of RNA-bound IFIT1 (PDB 6C6K (ref. 26), highlighting the difference in SD II orientation between IFIT1 and IFIT2/3 and the importance of SD II in IFIT1 for 5' cap binding. **f**, Evolutionary analyses of IFIT2 and IFIT3 across >20 rodent species, revealing codons evolving under purifying selection (red triangles, from FUBAR analysis) and positive selection (grey and black triangles, from FUBAR and PAML analyses, respectively).

To test whether IFIT2 and IFIT3 associate with the 5' regions of viral mRNAs during an endogenous IFN response, we performed eCLIP experiments in mouse embryonic fibroblasts (MEFs) in which *Ifit2* or *Ifit3a* and *Ifit3b* had been knocked out (Fig. 4c,d) and Extended Data Fig. 4c,d). In WT MEFs induced with IFN, IFIT2 and IFIT3 crosslinked with RNA sequences near the start codons of VSV mRNAs and showed an enrichment of viral mRNAs in the eCLIP dataset. In contrast, this association was lost when either *Ifit2* or *Ifit3a* and *Ifit3b* were knocked out. Although there are differences between our data with ectopically expressing cells and IFN-induced cells, we observe a similar overall pattern in IFIT2 and IFIT3 association with the 5' ends of VSV mRNAs and a necessity for both IFIT2 and IFIT3 together during the antiviral response. These data further support the observation that the IFIT2–IFIT3 complex associates with viral mRNAs near their start codons during an innate immune response in infected cells.

The IFIT2–IFIT3 complex inhibits translation of mRNAs with short viral 5' UTRs

Our eCLIP data indicate that the IFIT2–IFIT3 complex interacts with mRNA sequences downstream of the 5' cap (Fig. 4b,d). We therefore reasoned that viral genes may be sensitive to IFIT2–IFIT3-mediated inhibition even when expressed from a transfected plasmid. However, despite cloning the 5' UTR and open reading frame (ORF) of VSV-N, -P, -M, -G and -L, which contain the sequences bound by IFIT2–IFIT3 in our eCLIP experiments, we did not observe changes in viral protein levels in the presence of IFIT2–IFIT3 expression (Fig. 5a).

We next considered features of VSV mRNAs beyond their sequence that could differentiate them from most host mRNAs. One obvious difference is the vast discrepancy in 5' UTR length between VSV mRNAs (10–41 nt) and human mRNAs (median length of 218 nt)⁴³. We therefore hypothesized that 5' UTR length might serve as a molecular pattern for viral mRNA recognition by IFIT2–IFIT3. Using 5' rapid

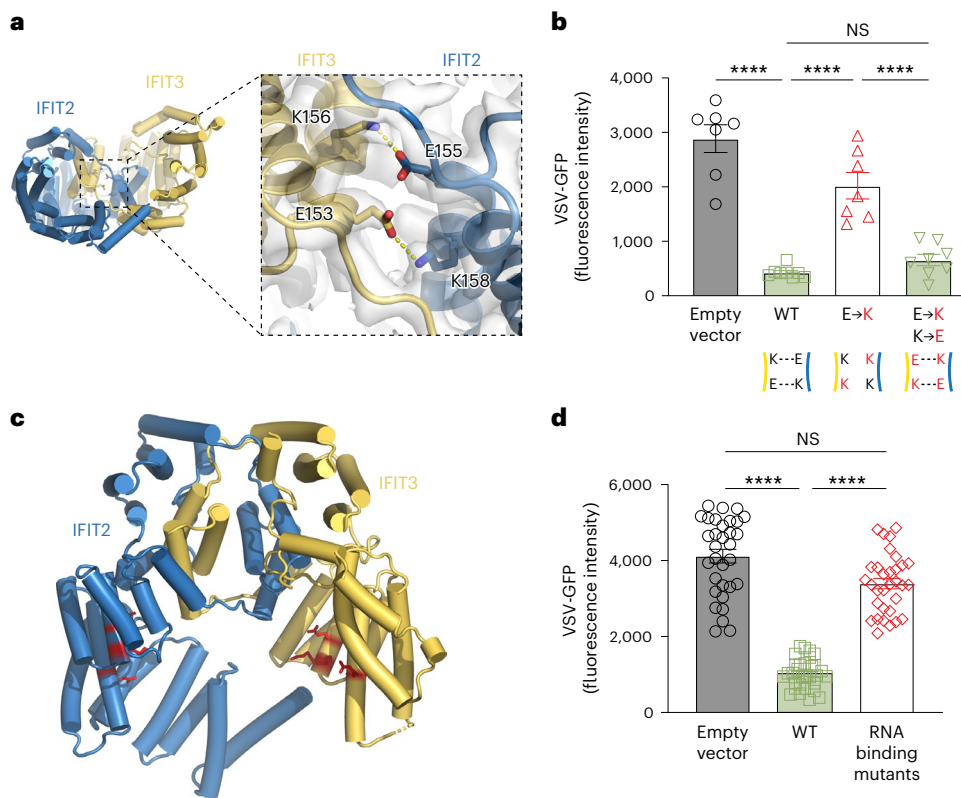


Fig. 3 | Structure-guided mutations of IFIT2 and IFIT3 abrogate antiviral activity. **a**, Zoomed-in view of the central helices in SD II that form a reciprocal salt bridge between IFIT2 (blue) and IFIT3 (yellow). Residue numbers are indicated. **b**, Importance of salt bridge residues for antiviral activity. HEK293T cells were transiently transfected with empty vector, wild-type (WT) IFIT2 and IFIT3, single E→K mutant IFIT2 (E155K) and IFIT3 (E153K), or double mutant E→K/K→E IFIT2 (E155K K158E) and IFIT3 (E153K K156E). At 24 h post transfection, cells were infected with VSV-GFP (0.05 MOI), and fluorescence images were taken

and quantified at 16 hpi ($n = 7$ biological replicates). **c**, Previously described RNA-binding residues^{37,42} (red) mapped on the IFIT2-IFIT3 heterodimer define a heterodimeric RNA-binding surface. **d**, RNA-binding mutants (mouse IFIT2: R250E, C253E, K254E, R287E; mouse IFIT3: Q249E, K252E, K253E, R286E) were tested for antiviral activity as described in **b** ($n = 4$ biological replicates, 32 technical replicates). In **b** and **d**, data are represented as mean ± s.e.m. and were analysed with an ordinary one-way ANOVA with Tukey's multiple comparisons test. **** $P < 0.0001$.

amplification of cDNA ends (RACE), we first determined that the transcription start site (TSS) of our plasmid was 105 nt upstream of where we cloned our viral sequences, resulting in a much longer 5' UTR than natural VSV mRNAs (Fig. 5a and Extended Data Fig. 5a). Strikingly, when we removed the majority of this extraneous sequence (Fig. 5b and Extended Data Fig. 5b), we observed strong sensitivity of VSV-N, -P, -G and -L protein expression when IFIT2-IFIT3 was expressed (Fig. 5b). These data, which recapitulate the decreased protein expression during viral infection when IFIT2-IFIT3 is expressed (Fig. 1e), suggest that 5' UTR length determines the sensitivity of an mRNA to IFIT2-IFIT3-mediated inhibition.

To facilitate more quantitative and high-throughput experiments, we established a fluorescence-based reporter assay. We first cloned GFP as a C-terminal fusion to VSV-P in our 'long' (105-nt plasmid-derived UTR followed by 10-nt VSV-P 5' UTR) and 'short' (3 nt followed by 10-nt VSV-P 5' UTR alone) plasmids (Fig. 5c). Consistent with our western blotting data (Fig. 5a,b and Extended Data Fig. 5c), GFP fluorescence signal was significantly decreased only when it was expressed with a 'short' 5' UTR and IFIT2-IFIT3 was co-expressed (Fig. 5d,e and Extended Data Fig. 5d).

Using this reporter assay, we next determined that only the 10-nt VSV-P 5' UTR, but not any part of the viral ORF, is required to sensitize GFP to repression by IFIT2-IFIT3 (Fig. 5f,g). Importantly, this sensitivity to IFIT2-IFIT3 expression was lost when the viral 5' UTR was lengthened to include the original 105-nt plasmid-derived UTR (Extended Data Fig. 6a), and neither IFIT2 nor IFIT3 alone inhibited translation of the VSV-P 5' UTR-alone construct (Extended Data Fig. 6b). We further confirmed that the observed inhibitory effect on protein

expression from the short 5' UTR was not due to IFIT-mediated changes in mRNA levels (Extended Data Fig. 6c) and confirmed that both human and mouse IFIT2-IFIT3 overexpression inhibited short 5' UTR reporter output in three different cell lines (Extended Data Fig. 6d). We also demonstrated that mutations in the dimer swap interface and predicted RNA-binding surfaces, which reduced antiviral activity (Fig. 3), also selectively impact the short but not long 5' UTR reporter (Extended Data Fig. 6e,f). Finally, we confirmed that the 5' UTRs from VSV-N, -M, -G and -L, which range from 10–41 nt, are all sensitive in our reporter system (Extended Data Fig. 6g), demonstrating that multiple viral 5' UTRs are susceptible to IFIT2-IFIT3-mediated mRNA translation inhibition.

Interestingly, in our eCLIP data, we also observed some host mRNAs that were bound in the 5' UTR region by IFIT2-IFIT3 (Extended Data Fig. 7). As with viral RNAs, we observed that IFIT2 and IFIT3 expression alone did not lead to substantial host RNA binding, and that the majority of host transcripts (>80%) bound by IFIT2-IFIT3 showed eCLIP peaks in the 5' end of the transcript (Extended Data Fig. 7a). Moreover, while the median human 5' UTR is >200 nt, there was an enrichment for IFIT2-IFIT3 binding to host transcripts with short (<50 nt) 5' UTRs, which were also predominantly bound in the 5' end (Extended Data Fig. 7b). Analysis of three such transcripts, with 5' UTRs ranging from 18–48 nt, showed clear eCLIP peaks at the 5' end only when IFIT2-IFIT3 were co-expressed (Extended Data Fig. 7c) and these same host 5' UTRs could sensitize GFP to inhibition by IFIT2-IFIT3 in our reporter system (Extended Data Fig. 7d). While the impact of IFIT2-IFIT3 on host mRNA

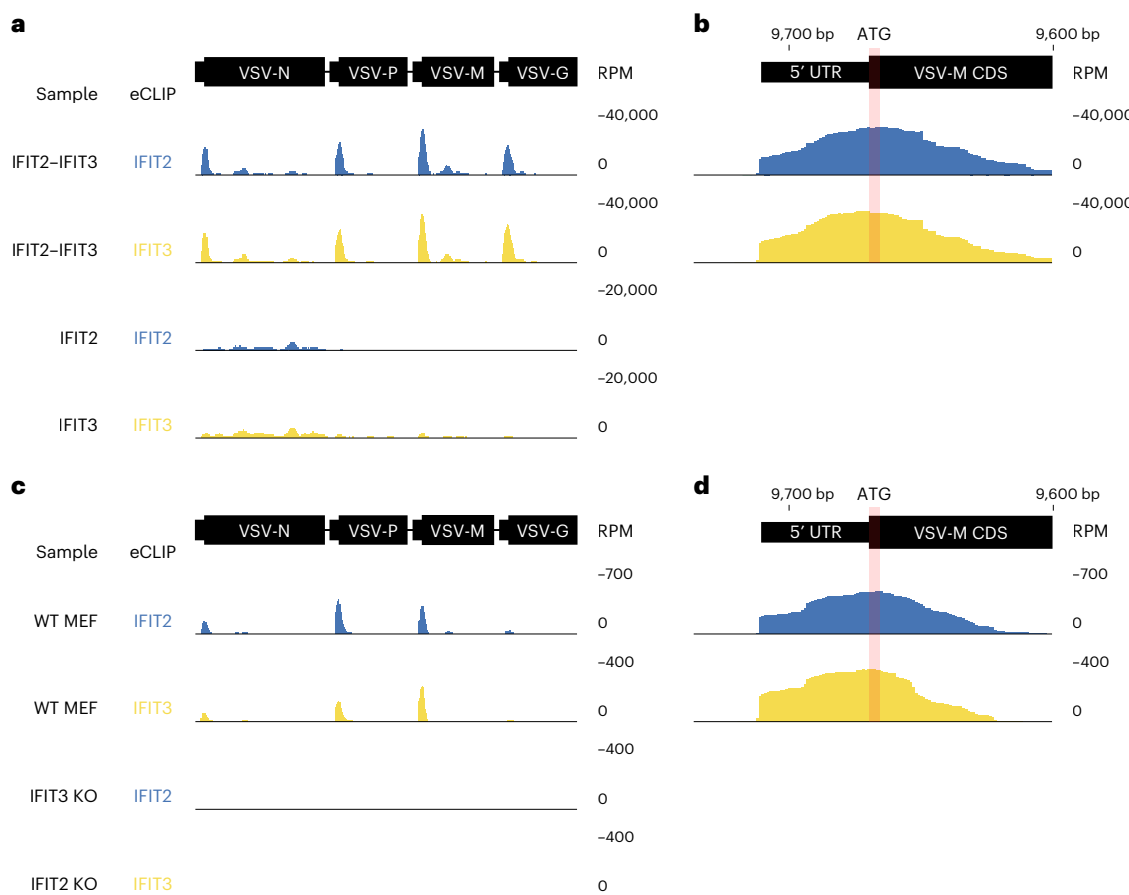


Fig. 4 | The IFIT2-IFIT3 heterodimer interacts with the 5' end of VSV mRNAs near the start codons. **a-d**, Browser tracks of VSV reads uniquely mapped to the viral genome as captured by eCLIP of IFIT2 or IFIT3 in (**a,b**) IFIT-expressing Flp-In T-REx HEK293 lines and (**c,d**) wild-type and *Ifit2* or *Ifit3* knockout MEFs.

eCLIP data are plotted as reads per million (RPM) mapped across the VSV genome normalized to the total RNA from that region of the viral genome. **b,d**, Zoomed-in browser tracks for 293 (**b**) and MEF (**d**) lines highlighting peaks of IFIT2-IFIT3 binding proximal to the start codon of the VSV-M gene.

translation remains to be fully explored, these data further support length-dependent inhibition by IFIT2-IFIT3.

The above data on viral and host transcripts show that 5' UTRs below a certain length are sensitive to IFIT2-IFIT3 inhibition. To identify the 5' UTR length threshold for IFIT2-IFIT3-mediated translation inhibition, we progressively added length to the sensitive 10-nt VSV-P 5' UTR, increasing it back to the complete plasmid-derived 105 nt (Fig. 5h). Using this approach, we demonstrated that the strongest IFIT2-IFIT3-mediated translation inhibition occurs when the total length of the 5' UTR is <50 nt (Fig. 5i).

IFIT2-IFIT3 has broad antiviral activity driven by the length of 5' UTRs

The data above suggest that a 5' UTR that is <50 nt in length can serve as a molecular pattern that sensitizes an mRNA to an IFIT2-IFIT3 complex. On the basis of this idea, we hypothesized that mRNA from other viruses with short 5' UTRs would be sensitive to IFIT2-IFIT3 antiviral activity. We first tested the 12–30-nt 5' UTRs from rabies virus (RABV), which is in the same *Rhabdoviridae* family as VSV, and found that all RABV UTRs are sensitive to IFIT2-IFIT3-mediated inhibition (Fig. 6a). These data are consistent with observations that RABV is more pathogenic in mice in which either *Ifit2* or *Ifit3* is knocked out^{21,23}.

We next tested another non-segmented negative-sense RNA virus with several short 5' UTRs, the human parainfluenza virus 3 (PIV3). PIV3 encodes two mRNAs with 5' UTRs <50 nt (gp5, 32 nt; gp8, 22 nt), both of which sensitize GFP to IFIT2-IFIT3-mediated inhibition in our reporter assay (Fig. 6b). As with VSV (Fig. 1b), neither IFIT2 nor IFIT3 alone exerted an antiviral effect on PIV3, but their co-expression significantly inhibited

infection (Fig. 6c). Moreover, as with VSV (Fig. 1a), knockdown of *Ifit2* and *Ifit3* expression in human A549 cells blunted the antiviral effects of type I IFN on PIV3 replication (Fig. 6d). Finally, we tested Sendai virus (SeV), a rodent paramyxovirus previously shown to be susceptible to inhibition by IFIT2 in mice⁴⁴. Similar to PIV3, SeV has several short 5' UTRs that we found to be sensitive in our reporter assay (Extended Data Fig. 8a), and viral replication is sensitive to IFIT2-IFIT3 overexpression but not overexpression of either IFIT2 or IFIT3 alone (Extended Data Fig. 8b). Together, our data on VSV, RABV, PIV3 and SeV indicate that IFIT2-IFIT3 co-expression confers inhibitory activity against diverse viruses that encode mRNAs with 5' UTRs shorter than 50 nt in length.

Finally, we evaluated whether a virus with a long 5' UTR would be insensitive to the antiviral effects of IFIT2 and IFIT3. We cloned the single 742-nt 5' UTR of coxsackievirus B3 (CVB3) upstream of GFP and tested it for sensitivity to IFIT2-IFIT3-mediated translation repression. Indeed, the CVB3 5' UTR was insensitive to IFIT2-IFIT3 expression, with reporter levels actually increasing (Fig. 6e), suggesting that IFIT2-IFIT3 may be proviral in some contexts as previously shown²⁷. Moreover, as predicted from our reporter assay data, ectopic expression of IFIT2 and IFIT3 did not inhibit CVB3 infection (Fig. 6f). These data suggest that viruses with long 5' UTRs may evade recognition and translation inhibition by the IFIT2-IFIT3 complex.

Discussion

Recognition of non-self viral mRNA is critical to controlling infection. Host cells must sense and distinguish viral mRNAs to prevent their translation and subsequent viral replication and formation of virions. Here we show that the interferon-stimulated genes (ISGs) IFIT2

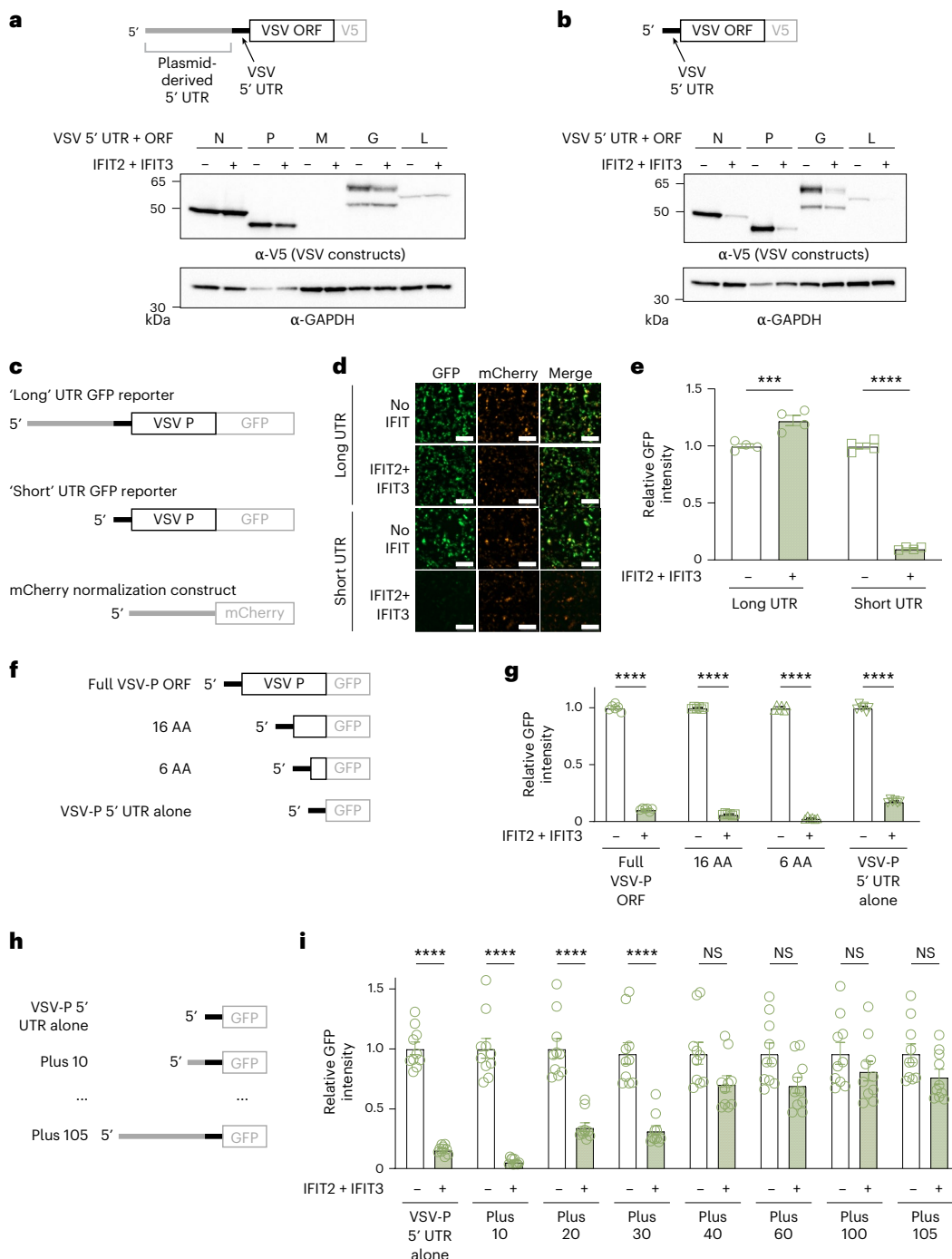


Fig. 5 | IFIT2-IFIT3 recognizes short viral 5' UTRs. **a**, The 5' UTR and ORF of each VSV gene was cloned into a mammalian expression plasmid fused to a C-terminal V5 tag (schematic at top). On the basis of 5' RACE data (Extended Data Fig. 5a), we identified a 108-nt plasmid-derived extension (grey) appended to the 5' end of the cloned VSV 5' UTR (black). Each viral gene-expressing construct was co-transfected in the absence or presence of IFIT2-IFIT3 into HEK293T cells. At 24 h post transfection, cells were collected and lysates were analysed by western blotting. **b**, Following plasmid engineering, only 3 nt of plasmid-derived sequence remained at the 5' end of each VSV UTR and ORF (schematic at top; Extended Data Fig. 5b). Transfections and western blotting were performed as in **a**. In **a** and **b**, experiments were performed independently at least twice. **c**, 5' UTR and ORF schematics for fluorescence reporter constructs shown in **d** and **e**. **d**, HEK293T cells were transfected with the indicated GFP reporters in the absence or presence of co-transfected IFIT2-IFIT3. All wells were transfected

with the control mCherry normalization construct. Images were taken at 24 h post transfection. Scale bars, 200 μ m. **e**, Experiments were performed as in **d**. For each well ($n = 4$ biological replicates), 4 images were taken and the ratio of GFP:mCherry signal intensity (Extended Data Fig. 5d) was calculated for each image. All values were normalized to the average of the condition in which IFIT2-IFIT3 was not transfected. **f**, 5' UTR and ORF schematics for GFP reporter constructs shown in **g**. AA, amino acids. **g**, Experiments with the indicated constructs were performed and quantified as in **e**. **h**, 5' UTR and ORF schematics for GFP reporter constructs shown in **i**. Plasmid-derived sequence from the 'long' construct shown in **c** was added back with the indicated number of nt (for example, Plus 10). **i**, Experiments with the indicated constructs were performed and quantified as in **e** ($n = 10$ biological replicates). For **e**, **g** and **i**, data are represented as mean \pm s.e.m. Statistical analyses: ordinary two-way ANOVA with Šídák's post test and a single pooled variance. **** $P < 0.0001$, *** $P = 0.0002$.

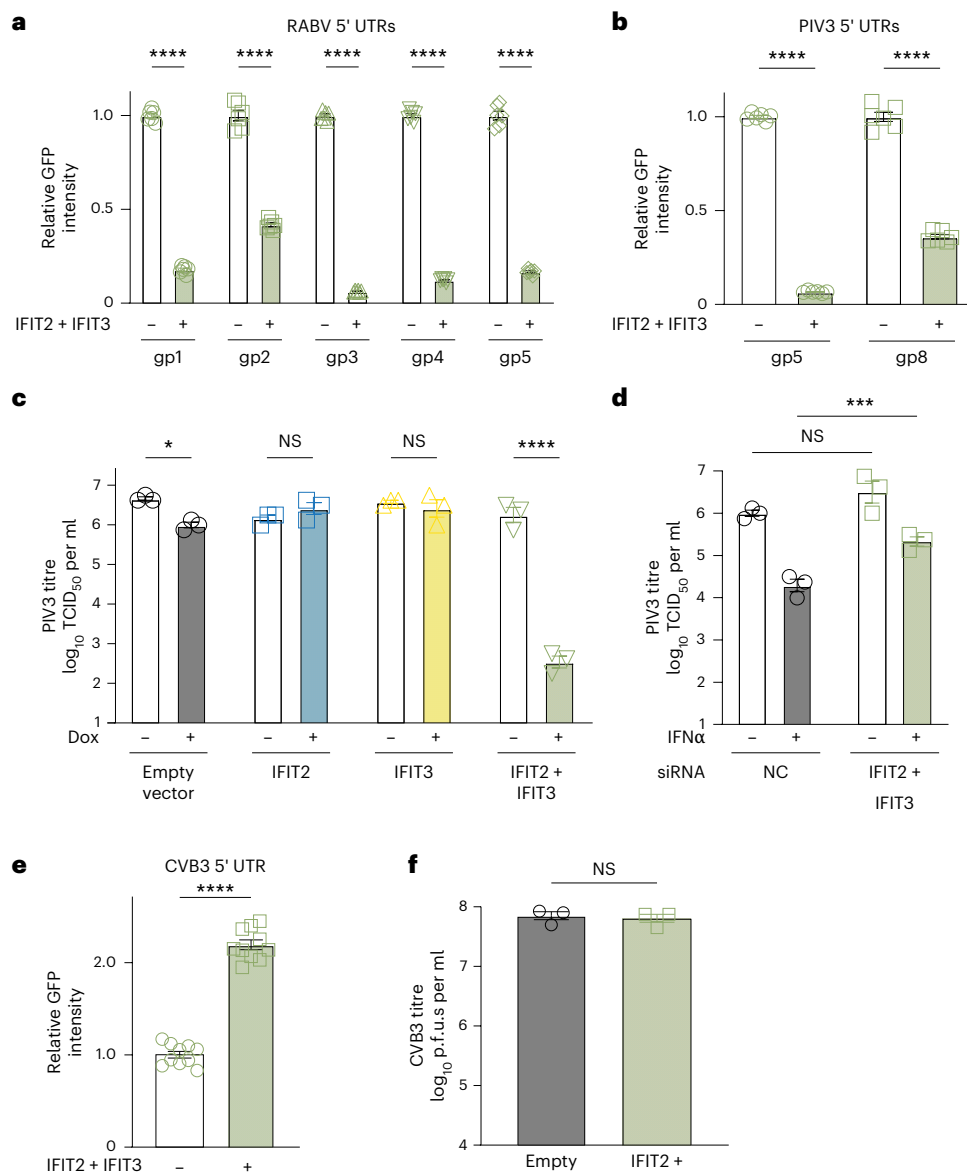


Fig. 6 | IFIT2-IFIT3 has broad antiviral activity driven by the length of 5' UTRs. **a,b**, HEK293T cells were transfected with GFP expression plasmids containing the indicated viral 5' UTRs from RABV (**a**) or PIV3 (**b**) in the absence or presence of co-transfected IFIT2-IFIT3. Experiments were performed as in Fig. 4e. **c**, Inducible Flp-In T-Rex HEK293 cells expressing no IFIT (black circles), IFIT2 (blue squares), IFIT3 (yellow triangles), or IFIT2 and IFIT3 together (green triangles) were mock treated or treated with doxycycline (500 ng μ l $^{-1}$) for 24 h and then infected with PIV3-GFP (0.1 MOI). Supernatant was collected at 48 hpi and quantified using TCID $_{50}$. **d**, A549 cells were treated with a non-targeting control siRNA (NC, black circles) as a negative control, or siRNA targeting *IFIT2* and *IFIT3* in combination (green diamonds). In indicated conditions, cells were induced with IFN α (1,000 U ml $^{-1}$). All cells were infected with PIV3-GFP (0.1 MOI), and supernatant

was collected at 48 hpi for quantification using TCID $_{50}$. **e**, HEK293T cells were transfected with a GFP expression plasmid containing the 742-nt CVB3 5' UTR in the absence or presence of co-transfected IFIT2-IFIT3. **f**, Inducible Flp-In T-Rex HEK293 cells expressing no IFIT (black circles), IFIT2 (blue squares), IFIT3 (yellow triangles), or IFIT2 and IFIT3 together (green triangles) were mock treated or treated with doxycycline (500 ng μ l $^{-1}$) for 24 h and then infected with CVB3 (0.1 MOI). Supernatant was collected at 24 hpi and titred. In **a-d**, all experiments were performed with 3 or more biological replicates, with individual datapoints shown. Data are represented as mean \pm s.e.m. Statistical analyses: ordinary two-way ANOVA with Šídák's multiple comparisons test and a single pooled variance (**a-d**); * $P < 0.05$, ** $P < 0.01$, *** $P < 0.001$; two-tailed unpaired parametric *t*-test (**e,f**); **** $P < 0.0001$.

and IFIT3 form a heterodimeric complex capable of exerting a potent antiviral effect against VSV (*Rhabdoviridae*) and both PIV3 and SeV (*Paramyxoviridae*), and that this activity is driven by recognition and translation inhibition of viral mRNAs containing short 5' UTRs.

RNA viruses have an average genome length of ~9 kilobases⁴⁵. With such limited genetic space, many viruses, especially small non-segmented negative strand RNA viruses, encode short 5' UTRs, presumably to maximize nucleotides available for protein-coding sequences. Although RNA viruses have high rates of mutation and can undergo rapid change to genome sequences^{46,47}, the length of

viral 5' UTRs is probably constrained due to limitations on overall genome size⁴⁶, enabling IFIT2 and IFIT3 to have evolved recognition of this feature as a hallmark of RNA virus infection. Indeed, nearly every non-segmented negative-sense RNA virus that infects humans contains at least one mRNA with a 5' UTR <50 nt, and our data with three of these viruses (PIV3, VSV and RABV) suggest that IFIT2-IFIT3 may be a broad restriction mechanism against them. However, our data revealing that the long 5' UTR of CVB3 and CVB3 infection are insensitive to IFIT2-IFIT3 expression, indicate that evolving longer viral 5' UTRs to mimic the length of host 5' UTRs is one potential viral

escape mechanism. Combined with studies showing that viruses can evolve RNA secondary structures, host-mimicking RNA methylation machinery and additional mechanisms to evade IFIT1 (refs. 16,20), these results suggest that IFITs may have had a profound effect on the evolution of the 5' ends of viruses. In addition, viruses have probably developed additional strategies to evade translation inhibition by IFIT2–IFIT3. As has been shown with IFIT1 (ref. 20), we find that primate and rodent IFIT2 and IFIT3 have evolved under strong recurrent positive selection, especially in SD III. These evolutionary data mirror the strong signatures of positive selection described for other antiviral ISGs that are targeted by viral antagonists^{16,20} and indicate that some viruses that otherwise might be sensitive to IFIT2–IFIT3-mediated repression probably encode species-specific IFIT antagonists.

Intriguingly, we find that IFIT2–IFIT3 can also recognize host mRNAs with short 5' UTRs and can inhibit translation of mRNAs containing host-derived short 5' UTRs. These data suggest that, similar to many other antiviral effectors, IFIT2–IFIT3 may not perfectly distinguish viral from host mRNAs and therefore may have a role in host protein regulation. Indeed, several studies have indicated that IFIT2 and IFIT3 have host-regulatory functions^{27–31}, although it is unknown whether any of those are due to inhibition of host mRNAs with short 5' UTRs. Future research focusing specifically on host mRNA translation will need to be conducted to understand the consequences of IFIT2–IFIT3-mediated inhibition of host mRNA translation.

The precise mechanism by which the IFIT2–IFIT3 complex selectively inhibits translation of mRNAs with short 5' UTRs also requires further study. Previous models based on ribosome structures and functional data have described a 'blind spot' in the 5' 40–50 nt of human mRNAs, where efficient translation initiation occurs at the first start codon downstream of the blind spot⁴⁸. However, viruses with short 5' UTR-containing mRNAs are able to efficiently translate their proteins during infection. This paradox suggests that there are exceptions to the blind spot model and that viruses that express mRNAs with short 5' UTRs probably co-opt non-canonical translational pathways. Indeed, VSV translation initiation is strongly dependent on the large ribosomal subunit protein, RPL40 (eL40), whereas bulk cellular translation is not⁴⁹. Likewise, host mRNAs with short 5' UTRs can contain a specific sequence known as a TISU (translation initiator of short 5' UTR)^{50,51}, and rely on specific ribosomal proteins and initiation factors for efficient translation^{52,53}. The differential requirements for efficient translation of mRNAs with short 5' UTRs and the similarity of our <50-nt length cut-off for IFIT sensitivity to the 40–50-nt ribosome blind spot lead us to hypothesize that IFIT2 and IFIT3 selectively inhibit a specialized translation pathway required for short 5' UTRs, although further work will be required to understand this mechanism in depth.

In summary, our study identifies short mRNA 5' UTRs as a molecular pattern that mammalian hosts can use to selectively inhibit viral replication. This pattern is present in a wide range of viral mRNAs and is sufficient to sensitize an mRNA to translation inhibition by the IFIT2–IFIT3 antiviral complex. Thus, 5' UTR length is another point of conflict in the battle between viruses and hosts for mRNA translation control.

Methods

The research described in this paper complies with all relevant ethics regulations and was approved by UCSD Environment, Health and Safety (EH&S) under Biohazard Use Authorization No. 2215. Animal experiments were carried out in accordance with the recommendations in the Guide for the Care and Use of Laboratory Animals of the National Institutes of Health. The protocols were approved by the Institutional Animal Care and Use Committee at the Washington University School of Medicine (Assurance number A3381-01).

Cell culture and transient transfection

HEK293T cells, BHK-21 [C-13] cells and H1-HeLa cells were obtained from ATCC (CRL-3216, CCL-10 and CRL-1958, respectively) and grown

in complete medium containing DMEM medium (Gibco), 10% FBS, 100 U ml⁻¹ penicillin and 100 µg ml⁻¹ streptomycin (Gibco). For transient transfections, HEK293T, BHK-21 or H1-HeLa cells were seeded the day before transfection in a 24-well plate (Genesee) with 500 µl of complete media. Cells were transiently transfected with 500 ng of total DNA and 1.5 µl of TransIT-X2 (Mirus Bio) following manufacturer protocol.

For generation of inducible cell lines, sequences for mCherry, IFIT2, IFIT3, or IFIT2 and IFIT3 separated by a P2A site were cloned into the Flp-In vector pcDNAS/FRT/TO. Flp-In T-REx HEK293 cells (Invitrogen, R78007) maintained in 5 µg ml⁻¹ of blasticidin were transfected at 70% confluence with mCherry or IFIT constructs and the vector containing the Flp recombinase pOG44 in a 1:10 molar ratio using TransIT-X2 (Mirus Bio). After 1 day, cells were transferred to new dishes, and on the following day, hygromycin (100 µg ml⁻¹) was added to cells. Following selection, cells were maintained in 5 µg ml⁻¹ of blasticidin and 100 µg ml⁻¹ of hygromycin. For induction of mCherry or IFIT proteins, cells were treated with 500 ng ml⁻¹ of doxycycline for 24 h.

MEFs from *Ifit2*^{-/-} and *ΔIfit3a/b* mice were prepared from day 13.5–14.5 embryos according to published protocols⁵⁴. Isolated MEFs were maintained in DMEM supplemented with 10% heat-inactivated fetal bovine serum (FBS) (Cytiva), 100 U ml⁻¹ penicillin–streptomycin (Invitrogen), non-essential amino acids (Cellgro) and Glutamax (Gibco). Passage 0 (PO MEFs) were frozen or split 1:4 when ~80% confluent (~3 days). To generate transformed MEFs, 5 × 10⁶ P1 primary MEFs were transfected with 10 µg of a plasmid (SV2)⁵⁵ encoding the SV40 T antigen under control of a CMV promoter, using FuGene reagent (Promega) (3:1 µl FuGene to µg DNA ratio). Upon achieving confluence, MEF cultures were split 1:10. This process was repeated for ~10 passages, at which time the transformed MEFs were frozen or used for experiments.

IFIT small interfering (si)RNA knockdowns

Specific siRNAs against *ifit1* (Integrated DNA Technologies; 5'-UAGACGAACCCAAGGAGGCUCAGCUU-3'), *ifit2* (Horizon Discovery, M-012582-01-0050) and *ifit3* (Integrated DNA Technologies, TriFECTa RNAi kit - hs.Ri.IFIT3.13.1) were obtained from their respective manufacturers. A549 cells were seeded into 24-well plates. At 24 h after seeding, cells were transfected with 20 pmol of siRNA in Lipofectamine 2000 Transfection Reagent (Invitrogen) and allowed to incubate for 24 h before being used in subsequent infection experiments or being collected for western blot to validate knockdown efficiency.

Viral stocks and infections

VSV-GFP⁵⁶ was propagated in BHK cells. For siRNA experiments, siRNA-treated A549 cells in 24-well plates were induced with 500 U ml⁻¹ of IFN α for 24 h. Cells were then infected at a multiplicity of infection (MOI) of 0.01 for 16 h before collection, and virus was quantified by plaque assay. For ectopic overexpression experiments, Flp-In T-REx HEK293 cells in 24-well plates were induced with doxycycline for 24 h. Cells were then infected at an MOI of 0.01 for 16 h before collection, and virus was quantified by plaque assay. For high-MOI experiments, Flp-In 293 cells in 96-well (imaging) or 24-well (western blotting) plates were infected at an MOI of 3.0, and cells were collected or plates were imaged at 0, 2-, 4-, 6- and 8 h post infection. For evaluation of structure-guided mutations, 293T cells cultured in 24-well plates were transfected at 6 h post seeding with IFIT constructs. At 18 h post transfection, cells were infected at an MOI of 0.05 for 16 h before imaging.

For siRNA experiments with PIV3-GFP and SeV-F1R-GFP⁵⁷, siRNA-treated A549 cells in 24-well plates were induced with 500 U ml⁻¹ of IFN α for 24 h. Cells were then infected at an MOI of 0.01, and supernatant was collected at 40 hpi. Virus was quantified using 50% tissue culture infectious dose (TCID₅₀) analysis. For ectopic expression experiments, Flp-In T-REx HEK293 cells in 24-well plates were induced with doxycycline for 24 h before being infected at an MOI of 0.1 for 48 h (PIV3) or 42 h (SeV). Supernatant was then collected, and virus was quantified using TCID₅₀.

CVB3 stocks were generated by co-transfection of CVB3-Nancy infectious clone plasmids with a plasmid expressing T7 RNA polymerase as previously described⁵⁸. For ectopic overexpression experiments, Flp-In T-REx HEK293 cells in 24-well plates were induced with doxycycline for 24 h before being infected at an MOI of 0.1. Supernatant was collected at 40 hpi and quantified by plaque assay.

Western blotting and antibodies

At 24 h post transfection, cells were resuspended in supernatant and collected, followed by centrifugation for 5 min at 587 × g. Cell pellets were washed with 1× PBS and lysed with 1× Bolt LDS sample buffer (Life Technologies) containing 5% β-mercaptoethanol at 98 °C for 7 min. The lysed samples were centrifuged at 21,130 × g for 2 min, followed by loading into 4–12% Bolt Bis-Tris Plus Mini Protein Gels (Life Technologies) with 1× Bolt MOPS SDS Running Buffer (Life Technologies). Following electrophoresis, gels were wet transferred onto nitrocellulose membranes using a Mini Blot Module (Life Technologies). Membranes were blocked with PBS-T containing 5% bovine serum albumin (BSA) (Spectrum), followed by incubation with primary antibodies (1:1,000) for VSV-G [8G5F11] and VSV-N [10G4] (Kerafast), V5[D3H8Q] (Cell Signaling Technology), HA [3F10] (Roche), FLAG [M2] (Sigma), HaloTag (Promega), human IFIT1 [3G8] (Novus Biologicals) or GAPDH [14C10] (Cell Signaling Technology). Membranes were rinsed three times in PBS-T and then incubated with the appropriate HRP-conjugated secondary antibodies (1:10,000; goat anti-rabbit IgG, Bio-Rad; goat anti-mouse IgG, Bio-Rad; goat anti-rat IgG, Invitrogen). Membranes were rinsed again three times in PBS-T and developed with SuperSignal West Pico PLUS Chemiluminescent Substrate (Thermo Fisher). Blots were imaged on a Bio-Rad ChemiDoc MP using the Bio-Rad Image Lab Software suite (v.6.1.0).

Immunoprecipitations (IPs)

HEK293T cells were seeded in 6-well plates and transfected the next day with plasmids expressing the indicated IFITs (600 ng each). Cells were collected in PBS at 24 h post transfection and centrifuged at 8,500 × g for 5 min at room temperature. Cell pellets were then flash frozen in liquid nitrogen and stored at –80 °C. For immunoprecipitation, cells were thawed on ice and incubated for 15 min in 500 µl of lysis buffer [20 mM Tris-Cl (pH 8.0), 150 mM NaCl, 15 mM MgCl₂, 1% (v/v) Triton X-100, 1× Protease Inhibitor Mini Tablets (Thermo Scientific), 1 mM dithiothreitol and 4 U TURBO DNase (Invitrogen)]. Lysates were centrifuged at 500 × g for 5 min at 4 °C to pellet cell debris, and 440 µl of the supernatant was transferred to LoBind tubes (Eppendorf SE), while 50 µl of this supernatant was set aside to serve as ‘Input lysate’ control samples for immunoblots. Monoclonal anti-HA agarose beads (Sigma-Aldrich) were washed three times in 1 ml of lysis buffer, followed by centrifugation at 800 × g for 5 min at 4 °C and removal of the supernatant. A volume of 40 µl of a 1:1 agarose beads:lysis buffer mix was added to each LoBind tube containing lysate, followed by incubation on a rotator for 3.5 h at 4 °C. After incubation, samples were washed three times by centrifugation at 800 × g for 5 min 4 °C, discarding the supernatant and adding 1 ml of lysis buffer. After the final wash, the supernatant was discarded. To remove bound proteins from agarose beads, 100 µl of 2× LDS sample buffer (Life Technologies) containing 10% (v/v) 2-mercaptoethanol (Thermo Scientific) was added to the agarose beads. The same amount (100 µl) of 2× LDS sample buffer was added to input lysate control samples. Samples were heated at 98 °C for 7 min and centrifuged at maximum speed for 5 min. Samples were then loaded onto a 4–12% Bis-Tris gel (Invitrogen) and electrophoresed in 1× MOPS SDS running buffer (Invitrogen). Immunoblots for HA, FLAG, HaloTag, IFIT1 and GAPDH were performed as described above.

Plasmids, constructs and molecular cloning

The coding sequences of mouse IFIT2 (NCBI accession BC050835) and mouse IFIT3 (NCBI accession BC089563) were cloned separately into

the pcDNA5/FRT/TO backbone (Invitrogen) with an N-terminal 3×FLAG tag or the pQCXIP backbone (Takara Bio) with an N-terminal HA tag, respectively, and both were cloned into the pcDNA5/FRT/TO backbone (an N-terminal HA tag, followed by IFIT3, a P2A site, a 3×FLAG tag and IFIT2). IFIT2 and IFIT3 point mutants were generated using overlapping stitch PCR and cloned into their respective backbones. The 5' UTR and coding sequence for each VSV gene (GenBank accession number NC_038236.1) was cloned into the pQCXIP backbone with a C-terminal V5 tag. Following 5' RACE, ‘short’ 5' UTR constructs were generated by truncating the pQCXIP 5' UTR sequence. The ‘long’ and ‘short’ backbone constructs expressing VSV-P-V5 were used to further clone the VSV-P fluorescence reporter plasmids by subcloning GFP in between the VSV-P 5' UTR and V5 tag. The mCherry normalization construct was generated by subcloning mCherry and a C-terminal 3×FLAG tag into the pcDNA5/FRT/TO backbone. All additional reporter constructs (including VSV-P truncations, UTR length constructs and viral 5' UTRs [RABV (NCBI accession NC_001542)]; [PIV3 (NCBI accession NC_001796)]; [CVB3 (NCBI accession NC_038307)]; [SeV (NC_075392.1)]) were cloned using primers and inserted into the ‘short’ UTR reporter backbone upstream of GFP-V5. All generated plasmids were sequenced across the entire inserted region to verify that no mutations were introduced during the cloning process. Plasmids and primers used in this study can be found in Supplementary Table 3. Gene fragments were ordered from Twist Bioscience or Genscript. All newly created plasmids will be made available upon request.

Protein expression and purification

For expression of the IFIT2–IFIT3 complex, we cloned codon-optimized genes encoding *M. musculus Ifit2* and *Ifit3* into separate plasmid vectors for expression in *E. coli*, with *Ifit2* cloned into UC Berkeley Macrolab vector 2-BT (Addgene, 29666; ampicillin resistant) encoding a TEV protease-cleavable His6-tag, and *Ifit3* cloned into UC Berkeley Macrolab vector 13S-A (Addgene, 48323; spectinomycin resistant) with no tag.

Plasmids were co-transformed into *E. coli* Rosetta pLysS cells (EMD Millipore) and grown overnight at 37 °C in LB plus carbenicillin and spectinomycin. Saturated overnight cultures were used to inoculate six 1-l cultures of 2XYT media plus carbenicillin and spectinomycin, and cultures were grown at 37 °C with shaking at 180 r.p.m. to an optical density at 600 nm (OD₆₀₀) of 0.8. Protein expression was induced by the addition of 0.25 mM IPTG, then cultures were shifted to 20 °C and grown another 16 h with shaking. Cells were collected by centrifugation and resuspended in nickel wash buffer (20 mM Tris-HCl pH 7.5, 500 mM NaCl, 20 mM imidazole pH 8.0, 2 mM beta-mercaptoethanol and 10% glycerol).

For protein purification, resuspended cells were lysed by sonication (Branson Sonifier), then cell debris was removed by centrifugation at 17,013 × g in a JA-17 rotor in an Avanti J-E centrifuge (Beckman Coulter) for 30 min. Clarified lysate was passed over a nickel column (5 ml HisTrap HP, Cytiva) in nickel wash buffer, then bound protein was eluted with nickel elution buffer (20 mM Tris-HCl pH 7.5, 75 mM NaCl, 250 mM imidazole pH 8.0, 2 mM beta-mercaptoethanol and 10% glycerol). Eluted protein was concentrated and buffer exchanged into nickel elution buffer containing 20 mM imidazole (Amicon Ultra, EMD Millipore), and the His₆-tag on IFIT2 was cleaved by addition of 1:10 w/w ratio of purified TEV protease (S219V mutant, purified in-house from expression vector pRK793; AddGene, 8827)⁵⁹, followed by incubation at 4 °C for 48 h. The reaction mixture was passed over a nickel column to remove cleaved His₆-tags, uncleaved IFIT2 and His₆-tagged TEV protease. The flow-through was concentrated, then passed over a size exclusion column (Superdex 200 Increase, Cytiva) in size exclusion buffer (20 mM Tris-HCl pH 7.5, 150 mM NaCl and 1 mM dithiothreitol), and fractions containing both proteins were pooled and concentrated.

Cryo-EM grid preparation

Before use, UltrAuFoil 1.2/1.3 300 mesh grids were plasma cleaned for 12 s using a Solarus II plasma cleaner (Gatan). Purified IFIT2–IFIT3 at

3 mg ml⁻¹ was applied to the grid in a 3-μl drop within the environmental chamber adjusted to 4 °C temperature and ~95% humidity in a Vitrobot Mark IV system (Thermo Fisher). After a 4-s incubation, the grids were blotted with a blot force of 4 for 4 s; the sample was then plunged frozen into liquid nitrogen-cooled liquid ethane.

Cryo-EM data acquisition and image processing

All data were acquired at the UCSD Cryo-EM Facility on a Titan Krios G3 electron microscope (Thermo Fisher) operating at 300 kV and equipped with a Gatan BioContinuum energy filter. All images were collected at a nominal magnification of ×165,000 in EF-TEM mode (with a calibrated pixel size of 0.854 Å) on a Gatan K2 detector using a 20-eV slit width and a cumulative electron exposure of ~65 electrons Å⁻² over 50 frames (Supplementary Table 1). Data were collected automatically using EPU (Thermo Fisher) with aberration-free image shift with a defocus range of -1 to -2.5 μm. Data collection was monitored live using the cryoSPARC Live platform (Structura Bio)⁶⁰ where movies were patch motion corrected and patch contrast transfer function (CTF) estimated on the fly. Micrographs with a CTF estimation worse than 7 Å and/or a cumulative motion of more than 150 pixels were discarded.

An initial 484,841 particle picks were obtained with crYOLO⁶¹ picker using a general model, and these picks were imported into cryoSPARC⁶⁰. Particles were extracted with a box size of 384 pixels and Fourier cropped to 96 pixels at 3.34 Å per pixel. These particles were subjected to three rounds of two-dimensional (2D) classification, where classes with proteinaceous features were chosen to move forward. The selected particles were subjected to an ab initio reconstruction to generate a starting model and carried forward to a non-uniform (NU) refinement using C1 symmetry. These particles were then re-extracted at a box size of 384 pixels with a Fourier crop to 128 pixels (1.708 Å per pixel), and a second NU refinement was performed. The particle stack was then subjected two rounds of a 2-class heterogeneous refinement, with one volume being the volume from the previous NU refinement and the other volume from EMD-4877 (20S proteasome)⁶², followed by NU refinement. In each round, the particles that contributed to the best volume that resembled the IFIT2–IFIT3 dimer were selected. A final 3-class heterogeneous refinement was performed using two IFIT2–IFIT3 volumes and a 20S proteasome volume. The particles associated with the volume that showed the best secondary structure features was selected and NU refinement was performed, resulting in a 3.51-Å-resolution map. These particles were then re-extracted at a box size of 384 pixels with no Fourier cropping (0.854 Å per pixel) and then NU refined, resulting in a 3.57-Å-resolution map. Due to heterogeneity that was observed in the map, particles were then exported from cryoSPARC into RELION⁶³, where they were extracted at a box size of 256 with a Fourier crop of 64 (3.34 Å per pixel). These particles were subjected to a round of 2D classification in which obvious junk classes were discarded. Selected particles were then re-extracted at a box size of 384 (0.854 Å per pixel) and subjected to 3D auto refinement, CTF refinement and a second 3D auto refinement⁶⁴. The particles were then Bayesian particle polished⁶⁵ before another round of two 3D auto refinements and a CTF refinement. This final particle stack was then imported back into cryoSPARC for a final NU refinement that resulted in a 3.22-Å-resolution map (Supplementary Table 1). 3DFSC was used to calculate directional Fourier shell correlation analysis for the final map⁶⁶.

To generate a starting model, we used ModelAngelo⁶⁷ and supplied our final 3.22 Å map and sequence files for IFIT2 and IFIT3. This resulting model was then iteratively real-space refined using Phenix⁶⁸ and manually adjusted in COOT⁶⁹. After the final refinement, the model was checked for accuracy in COOT (Supplementary Table 1).

Evolutionary analyses

For evolutionary analyses of primate and rodent IFIT2 and IFIT3, Uniprot reference protein sequences for human IFIT2, human IFIT3,

mouse IFIT2 and mouse IFIT3 were used as a search query against NCBI's non-redundant (NR) database using tBLASTn⁷⁰. Searches were restricted to simian primates and the Muroidea superfamily of rodents respectively. For each species, the nucleotide sequence with the highest bit score was downloaded and aligned to the human or mouse ORF nucleotide sequence using MAFFT⁷¹ implemented in Geneious software (Dotmatics; [geneious.com](http://www.geneious.com)). Poorly aligning sequences or regions were removed from subsequent analyses. Accession numbers of final sequences used for analyses are provided in Supplementary Table 2. Using these aligned sequences, FUBAR⁷² was performed on [Datamonykey.org](http://datamonykey.org) using 50 grid points and a 0.5 concentration parameter of the Dirichlet prior to infer codons evolving under positive and negative selection. Codons with a posterior probability of 0.9 or higher are given in Supplementary Table 2. PAML⁷³ was used to infer gene-wide positive selection, as well as codon-based estimates of positive selection. Aligned sequences were analysed using the NS sites models, disallowing (M7) or allowing (M8) positive selection. The *P* value reported is the result of a chi-squared test on twice the difference of the log likelihood (lnL) values between the two models using two degrees of freedom. Analyses were performed using two models of frequency (F61 and F3×4), and both sets of values are reported in Supplementary Table 2. For each codon model, we confirmed convergence of lnL values by performing each analysis using two starting omega (dN/dS) values (0.4 and 1.5). Positively selected codons with a posterior probability >0.90 using a Bayes empirical Bayes (BEB) analysis and the F61 codon frequency model are provided in Supplementary Table 2.

eCLIP experimental methods

Flp-In T-REx HEK293 cells in 10-cm culture dishes were induced with doxycycline for 24 h. Cells were then infected at an MOI of 3.0, and dishes were crosslinked using a UV crosslinker (254 nm; CL-1000 from UVP/Analytik Jena) at 400 mJ cm⁻². Downstream sample processing and eCLIP were performed as previously described⁷⁴, using antibodies against FLAG (M2/F1804, Sigma) and HA (HA.11/901502, Biolegend) for 293T experiments, and IFIT2 (PA3-845, Thermo Fisher) and IFIT3 (ABF1048, Millipore) for MEF experiments. Most experiments were performed in biological duplicate, except for the uninfected 293T samples (which were single replicates).

eCLIP computational analysis

Standard processing of eCLIP data was performed as previously described⁷⁴, with mapping performed to a custom genome index that included both the VSV genome and either hg19 (for 293T experiments) or mm10 (for MEF experiments). Data (Fig. 3 and Extended Data Fig. 4) are plotted as normalized reads per million (RPM), where reads per million are normalized to density of reads mapped to viral and human genomes.

Generation of *Ifit3a/b* DKO mice

Wild-type C57BL/6J were commercially obtained from Jackson Laboratories (Strain 000664). To generate *Ifit3*-deficient mice, single guide RNAs (sgRNAs) were designed to target exon two in *Ifit3a* and *Ifit3b*. Two sgRNAs were chosen that target conserved sequences between *Ifit3a* and *Ifit3b*: sgRNA-4, 5'-ATTCACCTGGATTATTCTNGG-3'; and sgRNA-30, 5'-ATGGCACTTCAGCTGTGGANGG-3'. Two additional sgRNAs were chosen that target only *Ifit3a* due to polymorphisms: sgRNA-21, 5'-ATTCTCGACTGGCACCTNGG-3'; and sgRNA-22, 5'-ATTCG TCGACTGGTCACCTGNGG-3'. The sgRNAs were selected on the basis of their low off-target profile. Guide RNAs and Cas9 protein were complexed and electroporated concurrently into C57BL/6J zygotes. Using this approach, we identified a mouse that had both *Ifit3a* and *Ifit3b* targeted (22-nt and 20-nt frameshift deletions, respectively), two mice in which only *Ifit3a* was targeted (2-nt and 119-nt frameshift deletions), and two mice in which only *Ifit3b* was targeted (1-nt and 2-nt frameshift insertions). After genotyping and two rounds of backcrossing,

five founder lines (*Ifit3a* del22/*Ifit3b* del20, *Ifit3a* del2, *Ifit3a* del119, *Ifit3b* ins1 and *Ifit3b* ins2) were generated. The generation of gene-edited mice was accomplished with the aid of the Genome Engineering and iPSC Center, and the Department of Pathology Micro-Injection Core (Washington University School of Medicine).

5' RACE

HEK293T cells were maintained as described above and subcultured into 6-well plates (Genesee) in 2 ml of complete media at 24 h before transfection. Cells were transiently transfected with 2,500 ng of total DNA and 7.5 µl of TransIT-X2 (Mirus Bio) following manufacturer protocol. At 24 h post transfection, cells were collected and pelleted; cell pellets were washed with 1× PBS, pelleted again, and supernatant was aspirated. RNA was extracted from pellets using the Takara Bio NucleoSpin RNA Plus kit following manufacturer protocol. Downstream processing of RNA was performed using the Takara Bio SMARTer RACE 5'/3' kit according to manufacturer protocol.

Fluorescent reporter assay

Cells (HEK293T or inducible Flp-In lines) were maintained as described above and subcultured into 24-well plates for transfection. Transfections were performed as described above except for the addition of 100 ng of an mCherry-expressing DNA plasmid, resulting in 600 ng of total DNA transfected along with 1.8 µl of TransIT-X2. At 24 h post transfection, cells were imaged using the BioTek Cytation 5 cell imaging multimode reader. Four images were taken at fixed positions in each well using a ×20 objective lens, with each condition in two replicates; both GFP and RFP images were collected for each well position. Non-transfected wells were imaged for use in background subtraction. Images were preprocessed in the BioTek Gen5 Image Prime 3.1 software package (v.3.1.06) using the default rolling ball algorithm settings, and mean fluorescence values for GFP and RFP were quantified using the Gen5 software before being exported to Microsoft Excel 2019 (v.2507).

Image analyses

Normalized GFP intensity for each image was calculated in Microsoft Excel as follows: (experimental GFP signal–background GFP signal)/(experimental RFP signal–background RFP signal). Background GFP and RFP signals are the average of the quantified preprocessed values from 8 total images taken of non-transfected wells. Once the normalized GFP intensity was calculated for each image, we averaged the normalized GFP intensity of each set of four images (that is, for each well). Finally, we calculated the relative GFP intensity for each well by dividing the average normalized GFP intensity from each well by the average of the two IFIT-untreated wells, thus representing each data point as relative to 100%.

RT-qPCR

HEK293T cells were maintained as described above in 24-well plates. Cells were collected in 1× PBS and pelleted at 500 × g for 1 min. RNA was then extracted using the New England BioLabs Monarch Total RNA Miniprep kit according to manufacturer protocol. RNA (100 ng) was then subjected to reverse transcription using the Applied Biosystems High-Capacity cDNA Reverse Transcription kit according to manufacturer protocol. The resulting cDNA was then used to conduct quantitative PCR on the Applied Biosystems StepOnePlus machine with gene-specific primers (GFP-F, 5'-CCGACCACTACCAGCAGAA CAC-3'; GFP-R, 5'-GGACCATGTGATCGCGCTTCTC-3'; 18S-F, 5'- TCGCTC GCTCCTCTACTTG-3'; 18S-R, 5'- GCTGACCGGGTTGGTTTGATCTG-3') and the Luna Universal qPCR Master Mix according to manufacturer protocol.

Statistics and reproducibility

Statistical analyses and data visualization were performed using GraphPad Prism 10 (v.10.4.1). Tests were performed as indicated in figure

legends. All error bars represent s.e.m. No statistical method was used to predetermine sample size, but our sample sizes are similar to those reported in previous publications^{75,76}. No data were excluded from the analyses. The experiments were not randomized. Data distribution was assumed to be normal, but this was not formally tested. Data collection and analysis were not performed blind to the conditions of the experiments, and the investigators were not blinded to allocation during experiments and outcome assessment.

Reporting summary

Further information on research design is available in the Nature Portfolio Reporting Summary linked to this article.

Data availability

All data reported in this paper are available in the paper, extended data, or as associated source data files (Source Data 1 contains datapoints shown in graphs, Source Data 2 contains all unedited western blot images). The cryo-EM structure has been deposited under PDB 9MK9 and EMDB code EMD-48323. Structural maps and model files are available through figshare at <https://doi.org/10.6084/m9.figshare.28385627.v1> (ref. 77). Sequencing data from eCLIP experiment have been deposited in GEO record GSE284636. Source data are provided with this paper.

Materials availability

All unique materials/reagents generated in this study are available through the lead contact (M.D.D., mdaugherty@ucsd.edu) upon request. Recipients are only expected to pay for shipping costs and there is no limitation on access. Every attempt will be made to send materials/reagents within one month of the request.

References

1. Hur, S. Double-stranded RNA sensors and modulators in innate immunity. *Annu. Rev. Immunol.* **37**, 349–375 (2019).
2. Liu, G. & Gack, M. U. Distinct and orchestrated functions of RNA sensors in innate immunity. *Immunity* **53**, 26–42 (2020).
3. Schwartz, S. L. & Conn, G. L. RNA regulation of the antiviral protein 2'-5'-oligoadenylate synthetase. *Wiley Interdiscip. Rev. RNA* **10**, e1534 (2019).
4. Zhu, J., Ghosh, A. & Sarkar, S. N. OASL—a new player in controlling antiviral innate immunity. *Curr. Opin. Virol.* **12**, 15–19 (2015).
5. Chow, K. T., Gale, M. Jr & Loo, Y. M. RIG-I and other RNA sensors in antiviral immunity. *Annu. Rev. Immunol.* **36**, 667–694 (2018).
6. Xie, F. & Zhu, Q. The regulation of cGAS-STING signaling by RNA virus-derived components. *Virol. J.* **21**, 101 (2024).
7. Shinde, O. & Li, P. The molecular mechanism of dsDNA sensing through the cGAS-STING pathway. *Adv. Immunol.* **162**, 1–21 (2024).
8. Dvorkin, S., Cambier, S., Volkman, H. E. & Stetson, D. B. New frontiers in the cGAS-STING intracellular DNA-sensing pathway. *Immunity* **57**, 718–730 (2024).
9. Chemudupati, M. et al. From APOBEC to ZAP: diverse mechanisms used by cellular restriction factors to inhibit virus infections. *Biochim. Biophys. Acta Mol. Cell Res.* **1866**, 382–394 (2019).
10. Kawai, T. & Akira, S. The role of pattern-recognition receptors in innate immunity: update on Toll-like receptors. *Nat. Immunol.* **11**, 373–384 (2010).
11. Fensterl, V. et al. Interferon-induced Ifit2/ISG54 protects mice from lethal VSV neuropathogenesis. *PLoS Pathog.* **8**, e1002712 (2012).
12. Diamond, M. S. & Farzan, M. The broad-spectrum antiviral functions of IFIT and IFITM proteins. *Nat. Rev. Immunol.* **13**, 46–57 (2013).
13. Daugherty, M. D., Schaller, A. M., Geballe, A. P. & Malik, H. S. Evolution-guided functional analyses reveal diverse antiviral specificities encoded by IFIT1 genes in mammals. *eLife* <https://doi.org/10.7554/eLife.14228> (2016).

14. Pichlmair, A. et al. IFIT1 is an antiviral protein that recognizes 5'-triphosphate RNA. *Nat. Immunol.* **12**, 624–630 (2011).
15. Abbas, Y. M., Pichlmair, A., Gorna, M. W., Superti-Furga, G. & Nagar, B. Structural basis for viral 5'-PPP-RNA recognition by human IFIT proteins. *Nature* **494**, 60–64 (2013).
16. Hyde, J. L. et al. A viral RNA structural element alters host recognition of nonself RNA. *Science* **343**, 783–787 (2014).
17. Fensterl, V. & Sen, G. C. Interferon-induced Ifit proteins: their role in viral pathogenesis. *J. Virol.* **89**, 2462–2468 (2015).
18. Abbas, Y. M. et al. Structure of human IFIT1 with capped RNA reveals adaptable mRNA binding and mechanisms for sensing N1 and N2 ribose 2'-O methylations. *Proc. Natl Acad. Sci. USA* **114**, E2106–E2115 (2017).
19. Mears, H. V. & Sweeney, T. R. Mouse Ifit1b is a cap1-RNA-binding protein that inhibits mouse coronavirus translation and is regulated by complexing with Ifit1c. *J. Biol. Chem.* **295**, 17781–17801 (2020).
20. McDougal, M. B., De Maria, A. M., Nakahara, E., Boys, I. N. & Schoggins, J. W. IFIT1 is rapidly evolving and exhibits disparate antiviral activities across 11 mammalian orders. Preprint at *bioRxiv* <https://doi.org/10.1101/2024.05.13.593954> (2025).
21. Chai, B. et al. Murine Ifit3 restricts the replication of rabies virus both in vitro and in vivo. *J. Gen. Virol.* <https://doi.org/10.1099/jgv.0.001619> (2021).
22. Cho, H., Shrestha, B., Sen, G. C. & Diamond, M. S. A role for Ifit2 in restricting West Nile virus infection in the brain. *J. Virol.* **87**, 8363–8371 (2013).
23. Davis, B. M. et al. Ifit2 is a restriction factor in rabies virus pathogenicity. *J. Virol.* <https://doi.org/10.1128/JVI.00889-17> (2017).
24. Fensterl, V., Wetzel, J. L. & Sen, G. C. Interferon-induced protein Ifit2 protects mice from infection of the peripheral nervous system by vesicular stomatitis virus. *J. Virol.* **88**, 10303–10311 (2014).
25. Poddar, D. et al. The interferon-induced protein, IFIT2, requires RNA-binding activity and neuronal expression to protect mice from intranasal vesicular stomatitis virus infection. *mBio* <https://doi.org/10.1128/mbio.00568-24> (2024).
26. Johnson, B. et al. Human IFIT3 modulates IFIT1 RNA binding specificity and protein stability. *Immunity* **48**, 487–499 e485 (2018).
27. Tran, V. et al. Influenza virus repurposes the antiviral protein IFIT2 to promote translation of viral mRNAs. *Nat. Microbiol.* **5**, 1490–1503 (2020).
28. Stawowczyk, M., Van Scy, S., Kumar, K. P. & Reich, N. C. The interferon stimulated gene 54 promotes apoptosis. *J. Biol. Chem.* **286**, 7257–7266 (2011).
29. Chen, L. et al. Inhibition of proteasome activity induces aggregation of IFIT2 in the centrosome and enhances IFIT2-induced cell apoptosis. *Int. J. Biol. Sci.* **13**, 383–390 (2017).
30. Zhang, Y. et al. Curcumin induces apoptosis in human leukemic cell lines through an IFIT2-dependent pathway. *Cancer Biol. Ther.* **18**, 43–50 (2017).
31. Hsu, Y. L., Shi, S. F., Wu, W. L., Ho, L. J. & Lai, J. H. Protective roles of interferon-induced protein with tetratricopeptide repeats 3 (IFIT3) in dengue virus infection of human lung epithelial cells. *PLoS ONE* **8**, e79518 (2013).
32. Das Sarma, J. et al. Ifit2 deficiency restricts microglial activation and leukocyte migration following murine coronavirus (m-CoV) CNS infection. *PLoS Pathog.* **16**, e1009034 (2020).
33. Fleith, R. C. et al. IFIT3 and IFIT2/3 promote IFIT1-mediated translation inhibition by enhancing binding to non-self RNA. *Nucleic Acids Res.* **46**, 5269–5285 (2018).
34. Schindewolf, C. et al. SARS-CoV-2 uses nonstructural protein 16 to evade restriction by IFIT1 and IFIT3. *J. Virol.* <https://doi.org/10.1128/jvi.01532-22> (2023).
35. Mears, H. V. & Sweeney, T. R. Better together: the role of IFIT protein–protein interactions in the antiviral response. *J. Gen. Virol.* <https://doi.org/10.1099/jgv.0.001149> (2018).
36. Fensterl, V. & Sen, G. C. The ISG56/IFIT1 gene family. *J. Interferon Cytokine Res.* **31**, 71–78 (2011).
37. Yang, Z. et al. Crystal structure of ISG54 reveals a novel RNA binding structure and potential functional mechanisms. *Cell Res.* **22**, 1328–1338 (2012).
38. Daugherty, M. D. & Malik, H. S. Rules of engagement: molecular insights from host–virus arms races. *Annu. Rev. Genet.* **46**, 677–700 (2012).
39. Sironi, M., Cagliani, R., Forni, D. & Clerici, M. Evolutionary insights into host–pathogen interactions from mammalian sequence data. *Nat. Rev. Genet.* **16**, 224–236 (2015).
40. Duggal, N. K. & Emerman, M. Evolutionary conflicts between viruses and restriction factors shape immunity. *Nat. Rev. Immunol.* **12**, 687–695 (2012).
41. Tenthorey, J. L., Emerman, M. & Malik, H. S. Evolutionary landscapes of host–virus arms races. *Annu. Rev. Immunol.* **40**, 271–294 (2022).
42. Sullivan, O. M. et al. IFIT3 RNA-binding activity promotes influenza A virus infection and translation efficiency. *J. Virol.* <https://doi.org/10.1128/jvi.00286-25> (2025).
43. Leppek, K., Das, R. & Barna, M. Functional 5' UTR mRNA structures in eukaryotic translation regulation and how to find them. *Nat. Rev. Mol. Cell Biol.* **19**, 158–174 (2018).
44. Wetzel, J. L., Fensterl, V. & Sen, G. C. Sendai virus pathogenesis in mice is prevented by Ifit2 and exacerbated by interferon. *J. Virol.* **88**, 13593–13601 (2014).
45. Holmes, E. C. *The Evolution and Emergence of RNA Viruses* (Oxford Univ. Press, 2009).
46. Holmes, E. C. Error thresholds and the constraints to RNA virus evolution. *Trends Microbiol.* **11**, 543–546 (2003).
47. Acevedo, A., Brodsky, L. & Andino, R. Mutational and fitness landscapes of an RNA virus revealed through population sequencing. *Nature* **505**, 686–690 (2014).
48. Brito Querido, J. et al. Structure of a human 48S translational initiation complex. *Science* **369**, 1220–1227 (2020).
49. Lee, A. S., Burdeinick-Kerr, R. & Whelan, S. P. A ribosome-specialized translation initiation pathway is required for cap-dependent translation of vesicular stomatitis virus mRNAs. *Proc. Natl Acad. Sci. USA* **110**, 324–329 (2013).
50. Elfakess, R. et al. Unique translation initiation of mRNAs-containing TISU element. *Nucleic Acids Res.* **39**, 7598–7609 (2011).
51. Elfakess, R. & Dikstein, R. A translation initiation element specific to mRNAs with very short 5'UTR that also regulates transcription. *PLoS ONE* **3**, e3094 (2008).
52. Sinvani, H. et al. Translational tolerance of mitochondrial genes to metabolic energy stress involves TISU and eIF1-eIF4GI cooperation in start codon selection. *Cell Metab.* **21**, 479–492 (2015).
53. Haimov, O. et al. Efficient and accurate translation initiation directed by TISU involves RPS3 and RPS10e binding and differential eukaryotic initiation factor 1A regulation. *Mol. Cell. Biol.* <https://doi.org/10.1128/MCB.00150-17> (2017).
54. Tan, Y. S. & Lei, Y. L. Generation and culture of mouse embryonic fibroblasts. *Methods Mol. Biol.* **1960**, 85–91 (2019).
55. Fischer-Fantuzzi, L., Scheidtmann, K. H. & Vesco, C. Biochemical properties of a transforming nonkaryophilic T antigen of SV40. *Virology* **153**, 87–95 (1986).
56. Boritz, E., Gerlach, J., Johnson, J. E. & Rose, J. K. Replication-competent rhabdoviruses with human immunodeficiency virus type 1 coats and green fluorescent protein: entry by a pH-independent pathway. *J. Virol.* **73**, 6937–6945 (1999).
57. Beaty, S. M. et al. Efficient and robust *Paramyxoviridae* reverse genetics systems. *mSphere* <https://doi.org/10.1128/mSphere.00376-16> (2017).

58. McCune, B. T., Lanahan, M. R., tenOever, B. R. & Pfeiffer, J. K. Rapid dissemination and monopolization of viral populations in mice revealed using a panel of barcoded viruses. *J. Virol.* **94**, e01590-19 (2020). <https://doi.org/10.1128/JVI.01590-19>
59. Kapust, R. B. et al. Tobacco etch virus protease: mechanism of autolysis and rational design of stable mutants with wild-type catalytic proficiency. *Protein Eng.* **14**, 993–1000 (2001).
60. Punjani, A., Rubinstein, J. L., Fleet, D. J. & Brubaker, M. A. cryoSPARC: algorithms for rapid unsupervised cryo-EM structure determination. *Nat. Methods* **14**, 290–296 (2017).
61. Wagner, T. et al. SPHIRE-crYOLO is a fast and accurate fully automated particle picker for cryo-EM. *Commun. Biol.* **2**, 218 (2019).
62. Toste Rego, A. & da Fonseca, P. C. A. Characterization of fully recombinant human 20S and 20S-PA200 proteasome complexes. *Mol. Cell* **76**, 138–147.e5 (2019).
63. Scheres, S. H. RELION: implementation of a Bayesian approach to cryo-EM structure determination. *J. Struct. Biol.* **180**, 519–530 (2012).
64. Zivanov, J., Nakane, T. & Scheres, S. H. W. Estimation of high-order aberrations and anisotropic magnification from cryo-EM data sets in RELION-3.1. *IUCrJ* **7**, 253–267 (2020).
65. Zivanov, J., Nakane, T. & Scheres, S. H. W. A Bayesian approach to beam-induced motion correction in cryo-EM single-particle analysis. *IUCrJ* **6**, 5–17 (2019).
66. Tan, Y. Z. et al. Addressing preferred specimen orientation in single-particle cryo-EM through tilting. *Nat. Methods* **14**, 793–796 (2017).
67. Jamali, K. et al. Automated model building and protein identification in cryo-EM maps. *Nature* **628**, 450–457 (2024).
68. Liebschner, D. et al. Macromolecular structure determination using X-rays, neutrons and electrons: recent developments in Phenix. *Acta Crystallogr. D Struct. Biol.* **75**, 861–877 (2019).
69. Emsley, P., Lohkamp, B., Scott, W. G. & Cowtan, K. Features and development of Coot. *Acta Crystallogr. D Biol. Crystallogr.* **66**, 486–501 (2010).
70. Altschul, S. F., Gish, W., Miller, W., Myers, E. W. & Lipman, D. J. Basic local alignment search tool. *J. Mol. Biol.* **215**, 403–410 (1990).
71. Katoh, K. & Standley, D. M. MAFFT multiple sequence alignment software version 7: improvements in performance and usability. *Mol. Biol. Evol.* **30**, 772–780 (2013).
72. Murrell, B. et al. FUBAR: a fast, unconstrained Bayesian approximation for inferring selection. *Mol. Biol. Evol.* **30**, 1196–1205 (2013).
73. Yang, Z. PAML 4: phylogenetic analysis by maximum likelihood. *Mol. Biol. Evol.* **24**, 1586–1591 (2007).
74. Blue, S. M. et al. Transcriptome-wide identification of RNA-binding protein binding sites using seCLIP-seq. *Nat. Protoc.* **17**, 1223–1265 (2022).
75. Tsu, B. V. et al. Host-specific sensing of coronaviruses and picornaviruses by the CARD8 inflammasome. *PLoS Biol.* **21**, e3002144 (2023).
76. Ryan, A. P., Delgado-Rodriguez, S. E. & Daugherty, M. D. Zinc-finger PARP proteins ADP-ribosylate alphaviral proteins and are required for interferon-gamma-mediated antiviral immunity. *Sci. Adv.* **11**, eadm6812 (2025).
77. Daugherty, M. IFIT2-IFIT3 CryoEM structural model and structural maps (associated with PDB 9MK9 and EMDB code EMD-48323). Dataset. figshare <https://doi.org/10.6084/m9.figshare.28385627.v1> (2025).

Acknowledgements

We thank L. A. VanBlargan for her contribution to the initial design and testing of *Ifit3*-deficient mice and cells; J. Rose (Yale University) for the generous gift of VSV-GFP, B. Lee (Icahn School of Medicine at

Mount Sinai) for providing PIV3-GFP and SeV-F1R-GFP, and J. Pfeiffer (University of Texas Southwestern Medical Center) for the CVB3-Nancy infectious clone plasmids; E. Bennett, A. Mehle, B. Lee and S. Cherry, as well as members of the Daugherty and Biering Labs, for helpful discussions; and P. Mitchell and S. Biering for comments on the paper. We acknowledge support from the National Institutes of Health (M.D.D.: K22 AI119017, R35 GM133633; E.L.V.N.: R00 HG009530; G.W.Y.: U24 HG009889, RF1 MH126719, R01 HG011864, R01 HG004659, subaward from U24 HG011735; B.L.: R01 AI188431; K.D.C.: R35 GM144121; S.K.: T32 GM133351), the Department of Defense/DARPA (B.L.: HERMES Program HR001124S0025-FP-005), and the Burroughs Wellcome Fund Investigators in the Pathogenesis of Infectious Disease Program (to M.D.D.). The funders had no role in study design, data collection and analysis, decision to publish, or preparation of the paper.

Author contributions

D.R.G. and M.D.D. conceptualized the project; D.R.G., C.T., A.D., E.E., J.D.W., M.A.H., E.L.V.N. and M.D.D. designed the methodology; D.R.G., C.T., B.C., S.K., A.D., E.E., J.D.W., C.T.H., P.F., J.P., K.S.H., B.A.Y., K.M.E., Q.L., S.R.H., J.B.C. and E.L.V.N. conducted investigations; D.R.G., M.D.B., K.D.C., E.L.V.N. and M.D.D. performed formal analysis; J.B.C., K.D.C. and M.S.D. procured resources; D.R.G., B.C., K.D.C. and M.D.D. wrote the original paper draft; all authors, except S.R.H. who has tragically passed away since making important initial discoveries for this work, reviewed and edited the paper; D.R.G., B.C., M.D.B., K.D.C., E.L.V.N. and M.D.D. performed visualization; K.D.C., M.S.D., B.L., G.W.Y., M.A.H., E.L.V.N. and M.D.D. supervised the project; M.D.D., E.L.V.N., G.W.Y., B.L. and K.D.C. acquired funding.

Competing interests

M.S.D. is a consultant or advisor for Inbios, Moderna, IntegerBio, Merck, GlaxoSmithKline, Bavarian Nordic, and Akagera Medicines. The Diamond laboratory has received unrelated funding support in sponsored research agreements from Emergent BioSolutions, Bavarian Nordic, Moderna, Vir Biotechnology, and IntegerBio. E.L.V.N. is co-founder, member of the Board of Directors, on the SAB, equity holder, and paid consultant for Eclipse BioInnovations, on the SAB of RNAConnect, and is inventor of intellectual property owned by University of California San Diego. E.L.V.N.'s interests have been reviewed and approved by the Baylor College of Medicine in accordance with its conflict-of-interest policies. G.W.Y. is a SAB member of Jumpcode Genomics and a co-founder, member of the Board of Directors, on the SAB, equity holder, and paid consultant for Eclipse BioInnovations. G.W.Y. is a visiting professor at the National University of Singapore. G.W.Y.'s interest(s) have been reviewed and approved by the University of California, San Diego in accordance with its conflict-of-interest policies. The other authors declare no competing interests.

Additional information

Extended data is available for this paper at <https://doi.org/10.1038/s41564-025-02138-w>.

Supplementary information The online version contains supplementary material available at <https://doi.org/10.1038/s41564-025-02138-w>.

Correspondence and requests for materials should be addressed to Matthew D. Daugherty.

Peer review information *Nature Microbiology* thanks Aartjan te Velthuis and the other, anonymous, reviewer(s) for their contribution to the peer review of this work.

Reprints and permissions information is available at www.nature.com/reprints.

Publisher's note Springer Nature remains neutral with regard to jurisdictional claims in published maps and institutional affiliations.

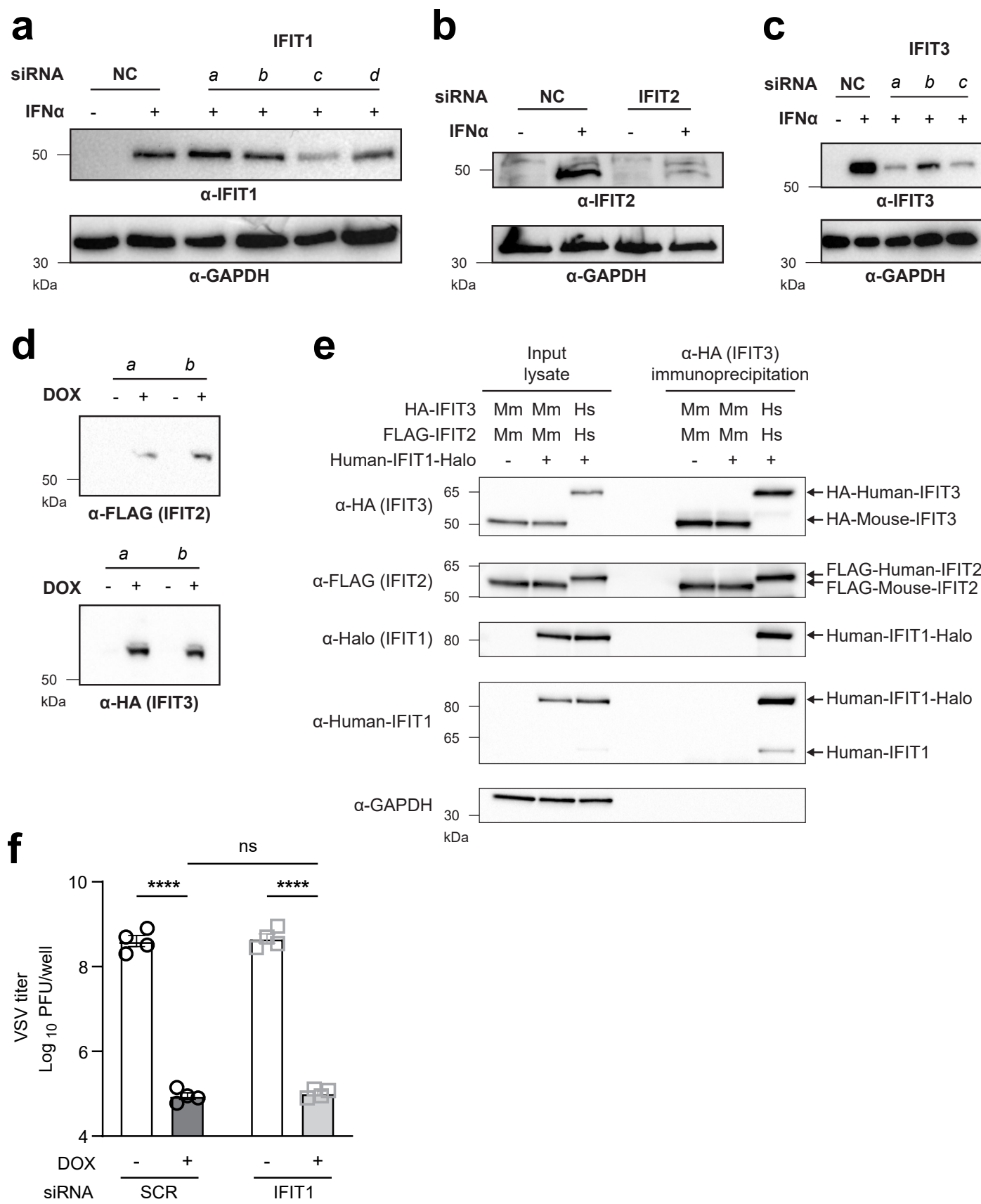
Open Access This article is licensed under a Creative Commons Attribution 4.0 International License, which permits use, sharing, adaptation, distribution and reproduction in any medium or format, as long as you give appropriate credit to the original author(s) and the source, provide a link to the Creative Commons licence, and indicate if changes were made. The images or other third party material in this

article are included in the article's Creative Commons licence, unless indicated otherwise in a credit line to the material. If material is not included in the article's Creative Commons licence and your intended use is not permitted by statutory regulation or exceeds the permitted use, you will need to obtain permission directly from the copyright holder. To view a copy of this licence, visit <http://creativecommons.org/licenses/by/4.0/>.

© The Author(s) 2025

¹School of Biological Sciences, University of California, San Diego, CA, USA. ²Department of Chemistry and Biochemistry, University of California, San Diego, CA, USA. ³Therapeutic Innovation Center, Baylor College of Medicine, Houston, TX, USA. ⁴Verna and Marrs McLean Department of Biochemistry and Molecular Pharmacology, Baylor College of Medicine, Houston, TX, USA. ⁵Department of Microbiology, Icahn School of Medicine at Mount Sinai, New York, NY, USA. ⁶Department of Cellular and Molecular Medicine, University of California, San Diego, CA, USA. ⁷Sanford Stem Cell Institute and Stem Cell Program, UC San Diego, La Jolla, CA, USA. ⁸Institute for Genomic Medicine, UC San Diego, La Jolla, CA, USA. ⁹Department of Molecular Microbiology, Washington University School of Medicine, St Louis, MO, USA. ¹⁰Department of Medicine, Washington University School of Medicine, St Louis, MO, USA. ¹¹Department of Pathology and Immunology, Washington University School of Medicine, St Louis, MO, USA.

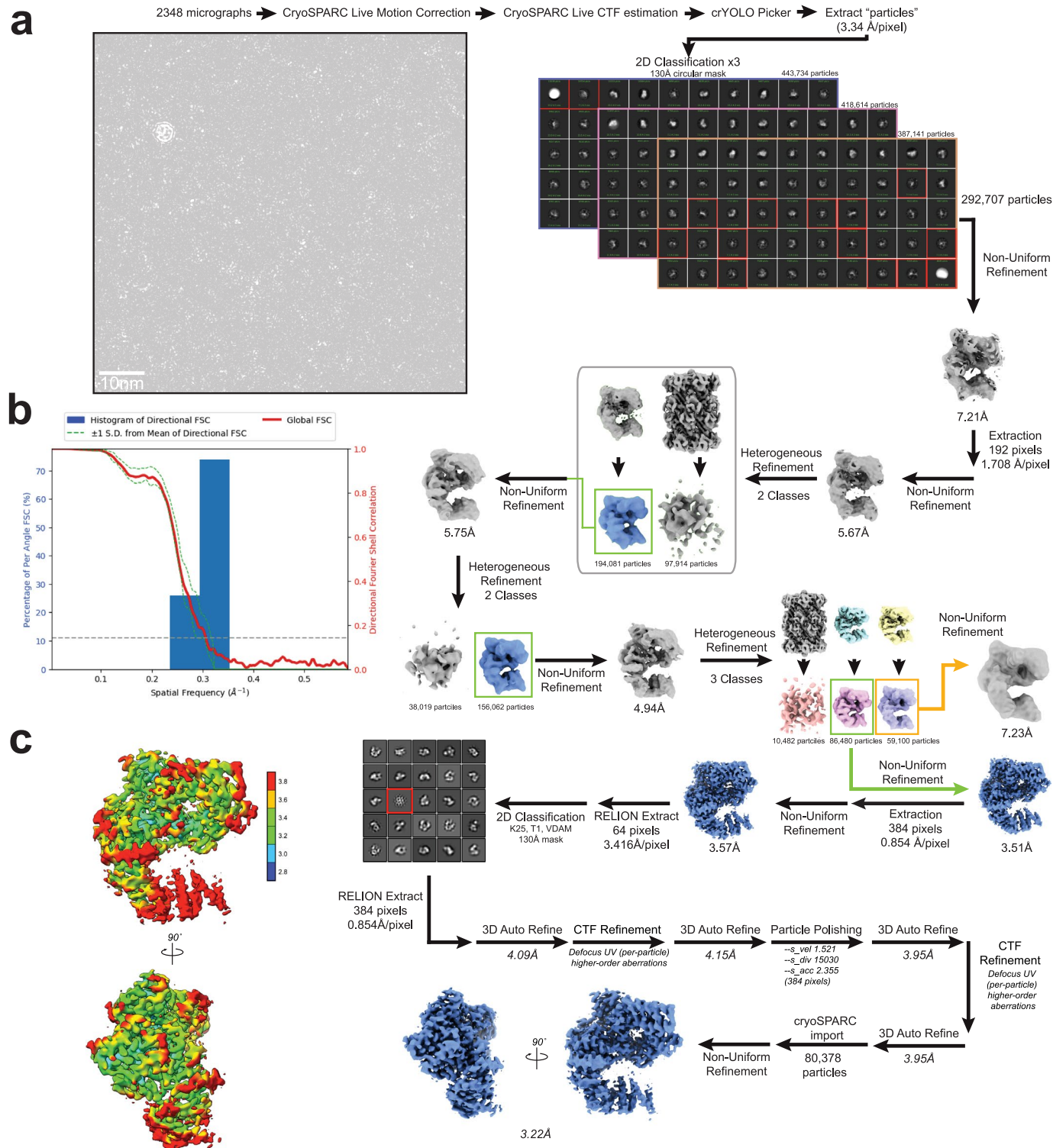
¹²Sanford Laboratories for Innovative Medicines, La Jolla, CA, USA.  e-mail: mddaugherty@ucsd.edu



Extended Data Fig. 1 | See next page for caption.

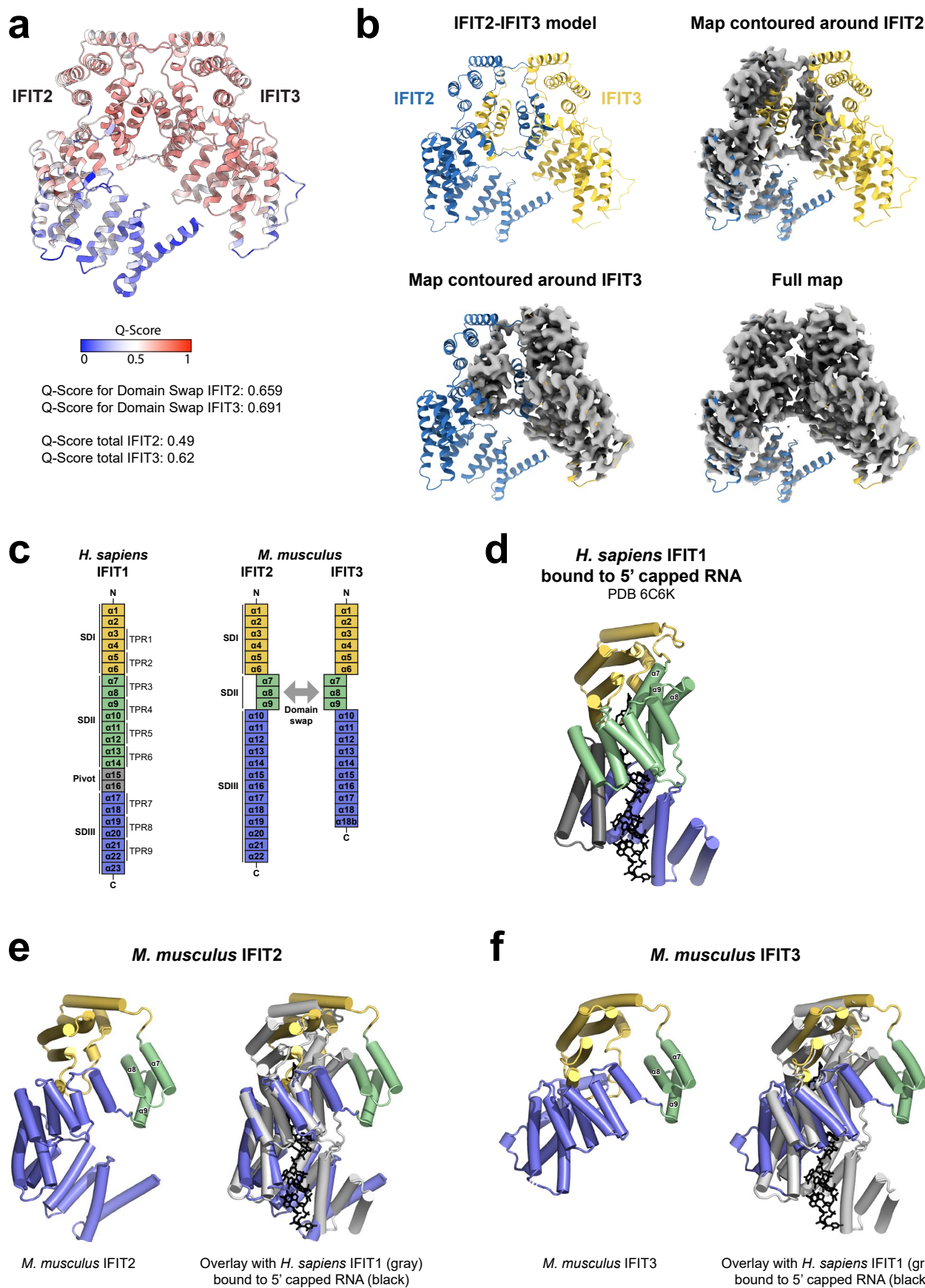
Extended Data Fig. 1 | siRNA knockdown of IFITs in A549 cells and expression of IFIT2 and IFIT3 in FlpIn lines, related to Fig. 1. (a–c) A549 cells were treated with a non-targeting siRNA as a negative control or siRNA targeting human (a) *IFIT1*, (b) *IFIT2*, or (c) *IFIT3*. Twenty-four hours post-treatment, cells were harvested and subsequently processed and analyzed by western blotting. Representative images shown; 2 independent experiments. For downstream infection experiments, siRNA IFIT1-c and siRNA IFIT3-a were used. (d) We generated inducible Flp-In T-REx HEK293 cell lines co-expressing mouse IFIT2 and IFIT3. Cells were induced with 500 ng/mL DOX for 24 h before harvesting cell pellets for analysis by western blot. Representative images shown; 2 independent experiments. For all associated downstream experiments, Flp-In line b was used. (e) HEK293T were transfected with the indicated epitope-tagged plasmids expressing IFIT proteins from human (Hs) or mouse (Mm) and subjected to immunoprecipitation with anti-HA conjugated beads to pull

down HA-tagged human or mouse IFIT3. With pulldown of mouse IFIT3, we observe strong pulldown of mouse IFIT2, but no endogenous or overexpressed human IFIT1, which is consistent with previous literature²⁶. In contrast, immunoprecipitation of human IFIT3 pulls down human IFIT2, and endogenous and overexpressed human IFIT1. Representative images shown; 2 independent experiments. (f) Inducible Flp-In T-REx HEK293 cells co-expressing mouse IFIT2 and IFIT3 were treated with a non-targeting control siRNA (NC, black circles) as a negative control or siRNA targeting IFIT1 (light grey squares). In indicated conditions, cells were mock treated or treated with doxycycline (500 ng μ l⁻¹) for 24 h and then infected with VSV-GFP (0.01 MOI), and supernatant was collected at 16 hpi for titration ($n = 4$ biological replicates). Statistical analyses: Data are represented as mean \pm SEM. Ordinary two-way ANOVA with Tukey's post-test and a single pooled variance. **** = $p < 0.0001$, ns = not significant.



Extended Data Fig. 2 | Cryo-EM data processing for IFIT2-IFIT3, related to Fig. 2. (a) Workflow for structure determination. See Methods for a detailed explanation of data processing. For 2D classes, classes outlined in red were excluded from later steps. For 3D classes, classes outlined in green were selected

for later steps. The final refined map showed a resolution of 3.22 Å (gold-standard FSC criterion of 0.143). (b) Directional Fourier Shell Correlation analysis for the final map, calculated by 3DFSC⁶⁶. (c) Two views of the final map, colored by local resolution (blue: 2.8 Å or better; red: 3.8 Å or worse).

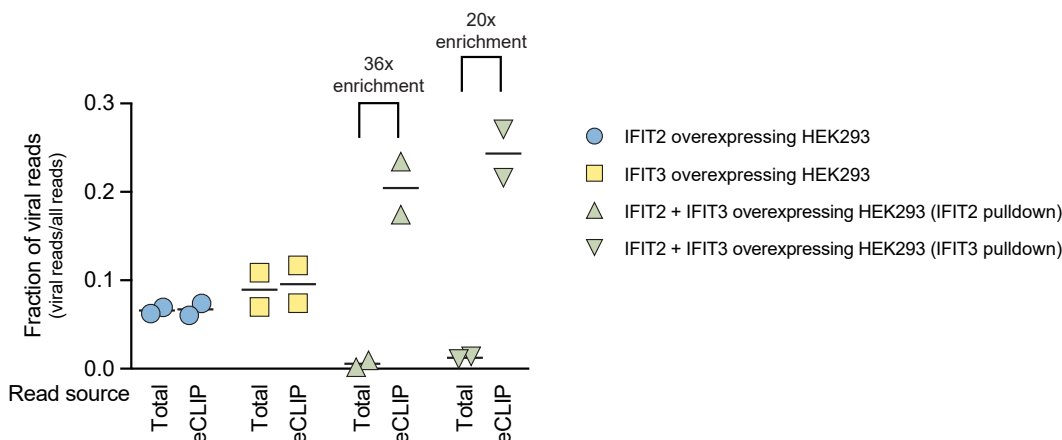
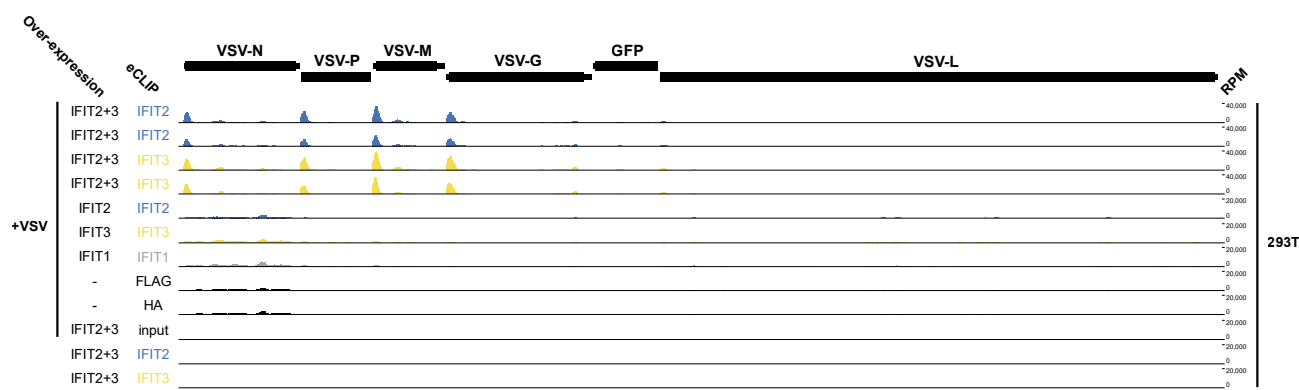
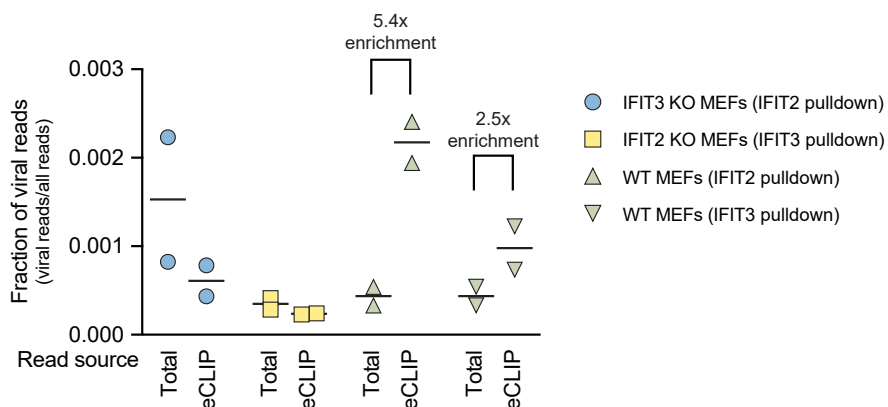
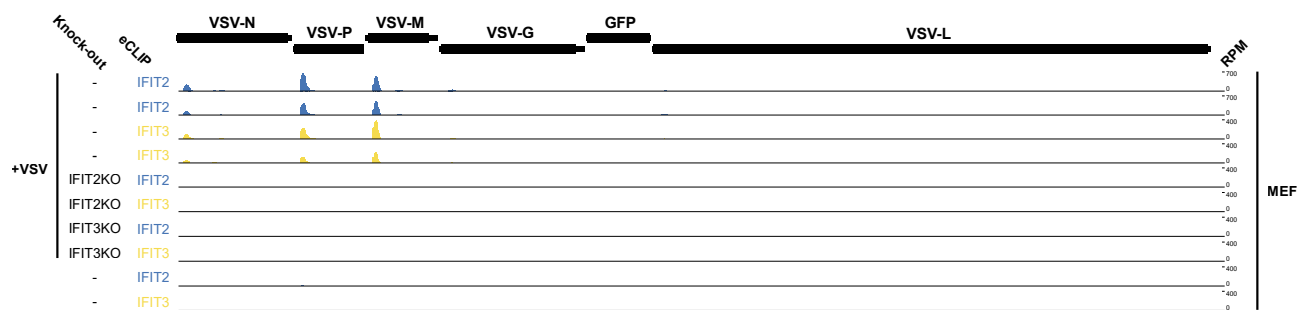


Extended Data Fig. 3 | See next page for caption.

Extended Data Fig. 3 | Comparison of IFIT structures, related to Fig. 2.

(a) Model of the IFIT2-IFIT3 heterodimer, colored by Q score, which measures the agreement of each residue with the experimental map. (b) IFIT2-IFIT3 model colored by protomer with IFIT2 blue and IFIT3 yellow, and experimental cryoEM map contoured around the IFIT2 protomer (top left), contoured around the IFIT3 protomer (bottom right), or showing the full map (bottom right). (c) Linear representation of human IFIT1 and mouse IFIT2 and IFIT3 domains showing

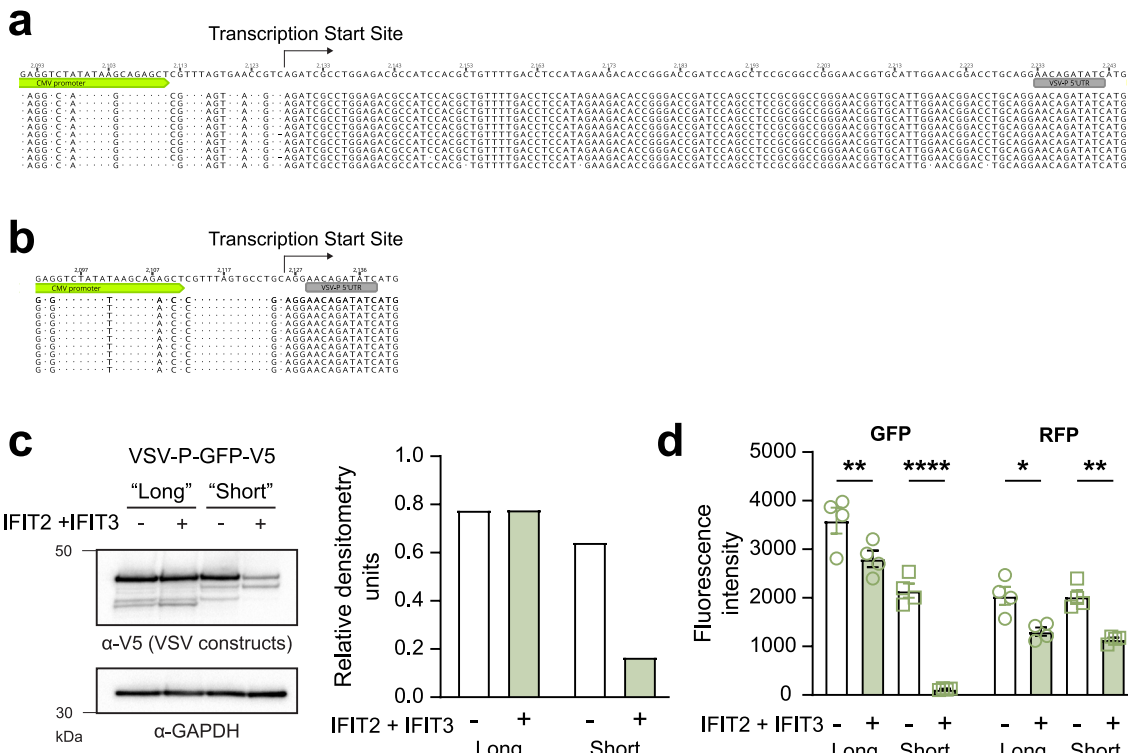
helix numbers and subdomains (SDs). (d) Structure of capped RNA-bound IFIT1 (PDB 6C6K ref. 26), colored by SD as in panel c. (e) (Left) Structure of mouse IFIT2 extracted from the IFIT2-IFIT3 heterodimer, colored by SD as in panel c. The green helices represent the domain-swapped helices during IFIT2-IFIT3 heterodimer formation. (Right) Mouse IFIT2 overlaid with IFIT1 (gray) bound to capped RNA (black). (f) Same as panel e, but with mouse IFIT3.

a**b****c****d**

Extended Data Fig. 4 | See next page for caption.

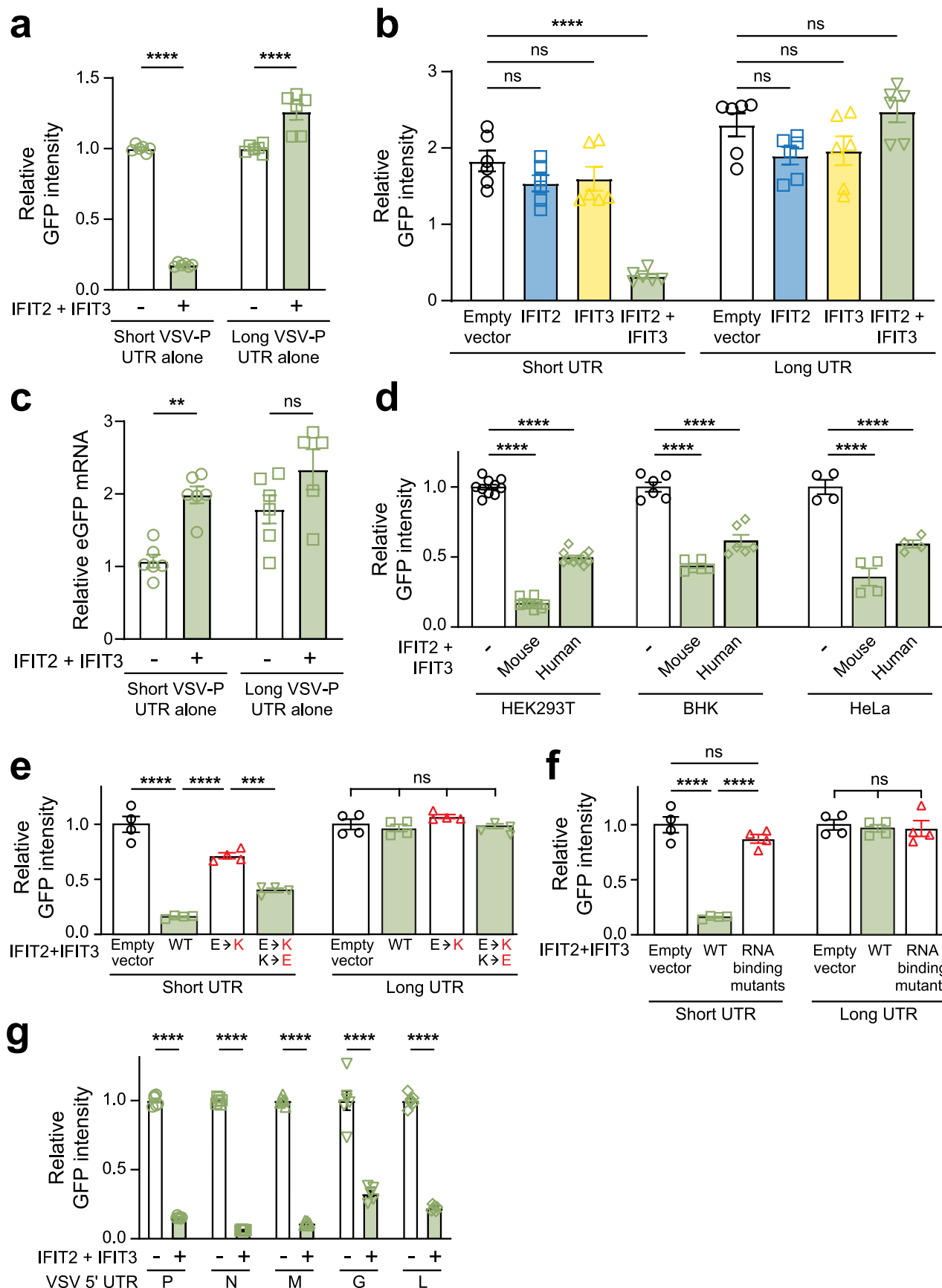
Extended Data Fig. 4 | Additional eCLIP data, related to Fig. 4. (a) Enrichment of VSV viral RNA in eCLIP samples from HEK293 cells overexpressing IFIT2-IFIT3. Fraction of viral RNA relative to all RNA (host+viral) from RNAseq (Total) and eCLIP (eCLIP) samples for each indicated VSV infected cell line. Each replicate is shown as a point, with the line showing the average fraction of viral reads. For IFIT2-IFIT3 overexpression, the fold enrichment of IFIT-bound (eCLIP) fraction relative to fraction of viral reads in RNAseq (Total) is indicated. (b) Full VSV

genome coverage for additional samples from the eCLIP experiment described in Fig. 4, including uninfected controls, for human IFIT-expressing Flp-In T-REx HEK293 lines. (c) Same as panel a, but for eCLIP samples from VSV infected mouse wild-type and *Ifit2* or *Ifit3* knockout MEFs. (d) Same as panel b, but for MEFs. (b, d) Values shown are normalized reads per million (RPM) out of all reads mapped to the VSV genome.



Extended Data Fig. 5 | IFIT2-IFIT3 recognizes short viral 5' UTRs, related to Fig. 5. (a-b) Plasmids expressing either a (a) long plasmid-derived 5' UTR or (b) no plasmid-derived 5' UTR immediately upstream of the VSV-P5' UTR were transfected into 293T cells. Twenty-four h post-transfection, cells were harvested, and RNA was isolated for 5' RACE experiments. Ten clones from each construct were sequenced, and the transcription start site is marked for each plasmid. (c) Experiment was carried out as described in Fig. 5c, but instead of

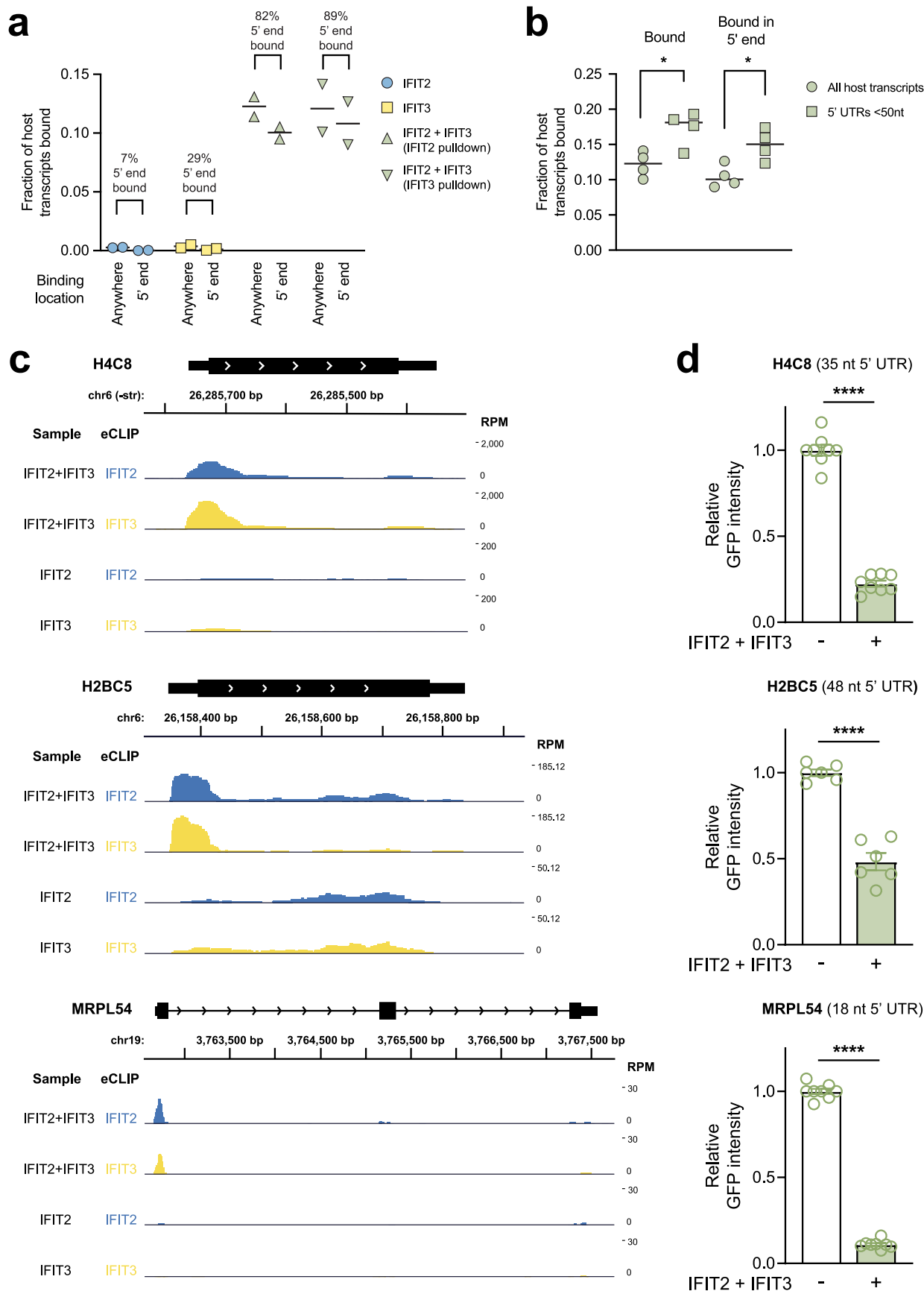
imaging, cells were harvested and lysates were analyzed by western blotting. Densitometry values were calculated using ImageJ. Experiment was performed independently twice. **(d)** Raw values from normalized data in Fig. 5d-e ($n = 4$ biological replicates). Statistical analyses: Data are represented as mean \pm SEM. **(d)** Ordinary two-way ANOVA with Šídák's multiple comparisons test and a single pooled variance. $^* = p < 0.05$, $^{**} = p < 0.01$, $^{****} = p < 0.0001$.



Extended Data Fig. 6 | See next page for caption.

Extended Data Fig. 6 | IFIT2-IFIT3 recognizes short viral 5' UTRs, related to Fig. 5. (a–b) 293T cells were transfected with plasmids expressing the 10 nt VSV-P 5' UTR and GFP with either a short or long plasmid-derived 5' UTR upstream of the viral sequence, co-transfected in the absence or presence of (a) IFIT2-IFIT3 or (b) IFIT2 or IFIT3 alone. Experiments were performed as described in Fig. 5f–g. (c) Cells were transfected as in panel a, and 22 h post-transfection, cells were harvested, RNA was extracted, and RT-qPCR was conducted with GFP mRNA levels normalized to 18S RNA levels. Data are pooled from two independent experiments, and data are expressed as relative to the short VSV-P UTR alone, no IFIT2-IFIT3 condition. (d) 293T (left), BHK (middle), and H1-Hela (right) cells were transfected with plasmids expressing the 10 nt VSV-P 5' UTR and GFP in the presence of empty vector (black circles), mouse IFIT2 and IFIT3 (green squares), or human IFIT2 and IFIT3 (orange diamonds). Experiments were performed as described in Fig. 5f–g. (e–f) 293T cells were transfected with plasmids expressing

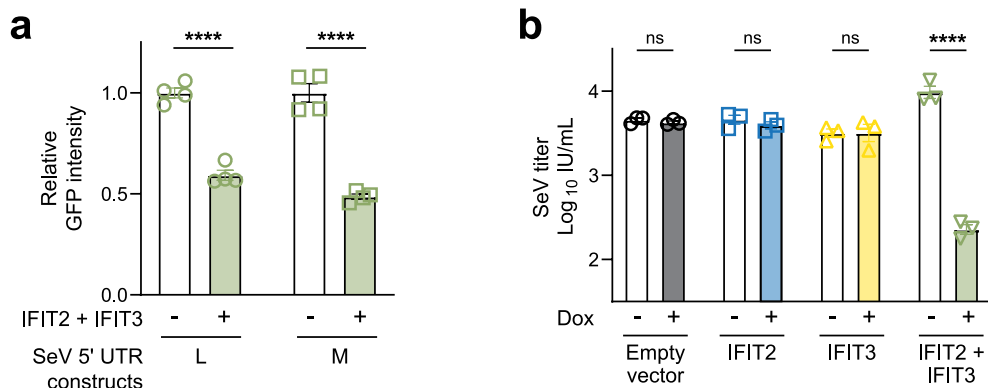
the 10 nt VSV-P 5' UTR and GFP with either a short (left) or long plasmid-derived (right) 5' UTR upstream of the viral sequence, co-transfected in the presence of empty vector (black circles), wild-type IFIT2-IFIT3 (green squares), (e) IFIT2-IFIT3 salt-bridge mutants (red triangles) and revertants (green triangles), or (f) IFIT2-IFIT3 RNA binding mutants (red triangles). Experiments were performed as described in Fig. 5g. (g) Cells were transfected with plasmids expressing GFP and the 5' UTR of each VSV gene in the absence or presence of IFIT2-IFIT3. Experiments were performed as described in Fig. 5g. Statistical analyses: Data are represented as mean \pm SEM. (a, b, c, g) Ordinary two-way ANOVA with Šídák's multiple comparisons test and a single pooled variance. ** = $p < 0.01$, *** = $p < 0.001$, **** = $p < 0.0001$, ns = not significant. (d, e, f) Ordinary one-way ANOVA with Tukey's multiple comparison test and a single pooled variance. Comparisons are to the empty vector condition within each column. ns = not significant, *** = $p < 0.001$, **** = $p < 0.0001$.



Extended Data Fig. 7 | See next page for caption.

Extended Data Fig. 7 | IFIT2-IFIT3 binds to host transcripts with short 5' UTRs, which can sensitize a reporter to IFIT2-IFIT3-mediated inhibition, related to Fig. 5. (a) Fraction of all host transcripts ($n \geq 10,000$ from RNAseq data) that eCLIP (greater than 3 in log10p and log2fc) with the indicated IFIT in VSV infected IFIT-overexpressing HEK293 cells. Transcripts with IFIT eCLIP signal in the 5' end of the transcript are shown. Each replicate is shown as a point, with the average indicated by a line. (b) Fraction of all host transcripts (circles) or host transcripts with 5' UTR lengths <50 nt (- 11% of all host transcripts) (squares) that are bound in VSV infected IFIT2-IFIT3 overexpressing cells. As in panel a, transcripts with IFIT eCLIP signal in the 5' end of the transcript are also shown. Individual replicates (combined from both IFIT2 and IFIT3 pulldowns) are shown as points, with the average value shown as a line. (c) Coverage of

three short 5' UTR-containing human genes (top: H4C8, 5' UTR AGGUUUUCUUAAGUUGGUUUAGAAGUUGCUUAGUC; middle: H2BC5, 5' UTR AUUAUUUUUCUCAGGUUGUUUGCAACAGUGUUUCUAACAUUAACGUACG; bottom: MRPL54, 5' UTR AAGCUGCCGCAAUACGUC) from the eCLIP experiment described in Fig. 4a-b. Values shown are normalized reads per million (RPM) out of all reads mapped to the human genome. (d) HEK293T cells were transfected with GFP expression plasmids containing the indicated human 5' UTRs from panel c in the absence or presence of co-transfected IFIT2-IFIT3. Experiments were performed as in Fig. 5e. Statistical analyses: Data are represented as mean \pm SEM. (b, d) Ordinary two-way ANOVA with Šidák's multiple comparisons test and a single pooled variance. * = $p < 0.05$, **** = $p < 0.0001$.



Extended Data Fig. 8 | IFIT2-IFIT3 inhibits replication of the murine Sendai Virus, related to Fig. 6. (a) HEK293T cells were transfected with GFP expression plasmids containing the indicated 5' UTRs from Sendai virus (SeV) in the absence or presence of co-transfected IFIT2-IFIT3. Experiments were performed as in Fig. 5e ($n = 4$ biological replicates). (b) Inducible Flp-In T-REx HEK293 cells expressing no IFIT (black circles), IFIT2 (blue squares), IFIT3 (yellow triangles), or IFIT2 and

IFIT3 together (green triangles) were mock-treated or treated with doxycycline ($500 \text{ ng} \mu\text{l}^{-1}$) for 24 h and then infected with SeV-F1R-EGFP (0.1 MOI). Supernatant was collected at 42 hpi for titration ($n = 3$ biological replicates). Statistical analyses: Data are represented as mean \pm SEM. (a, b) Ordinary two-way ANOVA with Šidák's multiple comparisons test and a single pooled variance. *** = $p < 0.0001$, ns = not significant.

Extended Data Table 1 | Evolutionary analysis, related to Fig. 2

Subdomain	Negatively-selected codons (FUBAR)	Positively-selected codons (FUBAR)	Positively-selected codons (PAML)	dN/dS	p-value for positive selection
Rodent IFIT2 - SD I	30	5	5	0.028	0.02
Rodent IFIT2 - SD II	16	0	0	0.11	1.0
Rodent IFIT2 - SD III	31	23	23	0.75	<0.0001
Rodent IFIT3 - SD I	22	3	4	0.37	0.009
Rodent IFIT3 - SD II	15	0	0	0.18	1.0
Rodent IFIT3 - SD III	23	12	12	0.69	<0.0001
Primate IFIT2 - SD I	15	7	5	0.33	0.03
Primate IFIT2 - SD II	6	0	0	0.12	1.0
Primate IFIT2 - SD III	28	12	8	0.54	<0.0001
Primate IFIT3 - SD I	20	2	2	0.28	0.013
Primate IFIT3 - SD II	5	0	0	0.18	1.0
Primate IFIT3 - SD III	25	7	7	0.69	<0.0001

Evolutionary analyses on subdomains of rodent and primate IFIT2 and IFIT3. Statistical evidence for positive selection, determined by PAML software, is shown for each gene and each subdomain, with statistically significant p-values shown in bold red text. The p-value reported is the result of a chi-squared test on twice the difference of the log likelihood ($\Delta\ln L$) values between the two PAML models of selection (M7 and M8) using two degrees of freedom. Overall dN/dS (omega) values for each subdomain are also shown. The number of specific codons within each subdomain that show statistical evidence for positive and negative selection, as determined by PAML and FUBAR software as indicated. Additional statistics and analysis parameters, complete lists of codons, and accession numbers and species of sequences analyzed are found in Supplementary Table 2.

Corresponding author(s): Matthew Daugherty

Last updated by author(s): Aug 18, 2025

Reporting Summary

Nature Portfolio wishes to improve the reproducibility of the work that we publish. This form provides structure for consistency and transparency in reporting. For further information on Nature Portfolio policies, see our [Editorial Policies](#) and the [Editorial Policy Checklist](#).

Statistics

For all statistical analyses, confirm that the following items are present in the figure legend, table legend, main text, or Methods section.

n/a Confirmed

- The exact sample size (n) for each experimental group/condition, given as a discrete number and unit of measurement
- A statement on whether measurements were taken from distinct samples or whether the same sample was measured repeatedly
- The statistical test(s) used AND whether they are one- or two-sided
Only common tests should be described solely by name; describe more complex techniques in the Methods section.
- A description of all covariates tested
- A description of any assumptions or corrections, such as tests of normality and adjustment for multiple comparisons
- A full description of the statistical parameters including central tendency (e.g. means) or other basic estimates (e.g. regression coefficient) AND variation (e.g. standard deviation) or associated estimates of uncertainty (e.g. confidence intervals)
- For null hypothesis testing, the test statistic (e.g. F , t , r) with confidence intervals, effect sizes, degrees of freedom and P value noted
Give P values as exact values whenever suitable.
- For Bayesian analysis, information on the choice of priors and Markov chain Monte Carlo settings
- For hierarchical and complex designs, identification of the appropriate level for tests and full reporting of outcomes
- Estimates of effect sizes (e.g. Cohen's d , Pearson's r), indicating how they were calculated

Our web collection on [statistics for biologists](#) contains articles on many of the points above.

Software and code

Policy information about [availability of computer code](#)

Data collection

Fluorescent images were captured, preprocessed, and quantified using the BioTek Gen5 Image Prime 3.1 Software for Imaging & Microscopy version 3.1.06. Western blots were imaged using the Bio-Rad Image Lab software version 6.1.0. qRT-PCR data were collected using the Applied Biosystems StepOnePlus machine.

Data analysis

Data analysis for virological assays and reporter assays was conducted using Microsoft Excel 2019 version 2507 and GraphPad Prism 10 version 10.4.1. Evolutionary analyses were performed with PAML (version 4.9), MAFFT (version 7.388), Geneious (version 2025.0.1), and FUBAR (Datammonkey online version).

For manuscripts utilizing custom algorithms or software that are central to the research but not yet described in published literature, software must be made available to editors and reviewers. We strongly encourage code deposition in a community repository (e.g. GitHub). See the Nature Portfolio [guidelines for submitting code & software](#) for further information.

Data

Policy information about [availability of data](#)

All manuscripts must include a [data availability statement](#). This statement should provide the following information, where applicable:

- Accession codes, unique identifiers, or web links for publicly available datasets
- A description of any restrictions on data availability
- For clinical datasets or third party data, please ensure that the statement adheres to our [policy](#)

All data reported in this paper are available in the manuscript, extended data, or as associated source data files (Source Data 1 contains datapoints shown in graphs, Source Data 2 contains all unedited western blot images). The cryo-EM structure has been deposited under PDB 9MK9 and EMDB code EMD-48323. Structural maps and model files are available through figshare at <https://doi.org/10.6084/m9.figshare.28385627.v1>. Sequencing data from eCLIP experiment have been deposited in GEO record GSE284636.

Research involving human participants, their data, or biological material

Policy information about studies with [human participants or human data](#). See also policy information about [sex, gender \(identity/presentation\), and sexual orientation](#) and [race, ethnicity and racism](#).

Reporting on sex and gender

Use the terms sex (biological attribute) and gender (shaped by social and cultural circumstances) carefully in order to avoid confusing both terms. Indicate if findings apply to only one sex or gender; describe whether sex and gender were considered in study design; whether sex and/or gender was determined based on self-reporting or assigned and methods used. Provide in the source data disaggregated sex and gender data, where this information has been collected, and if consent has been obtained for sharing of individual-level data; provide overall numbers in this Reporting Summary. Please state if this information has not been collected. Report sex- and gender-based analyses where performed, justify reasons for lack of sex- and gender-based analysis.

Reporting on race, ethnicity, or other socially relevant groupings

Please specify the socially constructed or socially relevant categorization variable(s) used in your manuscript and explain why they were used. Please note that such variables should not be used as proxies for other socially constructed/relevant variables (for example, race or ethnicity should not be used as a proxy for socioeconomic status). Provide clear definitions of the relevant terms used, how they were provided (by the participants/respondents, the researchers, or third parties), and the method(s) used to classify people into the different categories (e.g. self-report, census or administrative data, social media data, etc.) Please provide details about how you controlled for confounding variables in your analyses.

Population characteristics

Describe the covariate-relevant population characteristics of the human research participants (e.g. age, genotypic information, past and current diagnosis and treatment categories). If you filled out the behavioural & social sciences study design questions and have nothing to add here, write "See above."

Recruitment

Describe how participants were recruited. Outline any potential self-selection bias or other biases that may be present and how these are likely to impact results.

Ethics oversight

Identify the organization(s) that approved the study protocol.

Note that full information on the approval of the study protocol must also be provided in the manuscript.

Field-specific reporting

Please select the one below that is the best fit for your research. If you are not sure, read the appropriate sections before making your selection.

Life sciences Behavioural & social sciences Ecological, evolutionary & environmental sciences

For a reference copy of the document with all sections, see nature.com/documents/nr-reporting-summary-flat.pdf

Life sciences study design

All studies must disclose on these points even when the disclosure is negative.

Sample size

No statistical method was used to predetermine sample size but our sample sizes are similar to those reported in previous publications (Tsu et al. 2003. PLoS Biol; Ryan et al. 2025. Sci Adv.).

Data exclusions

No data were excluded from these analyses.

Replication

Experiments were performed multiple independent times, often by different researchers. All replication attempts were successful. Experiments were performed with a minimum of biological duplicate conditions, and each experiment was independently performed at least twice (for a total of at least 4 biological replicates).

Randomization

Experiments were not randomized, as this was not relevant to our study. Experiments were performed in the same cell line, where the tested conditions were -/+ viral infection, -/+ a reporter plasmid, and/or -/+ treatment with IFIT, interferon, or doxycycline.

Blinding

Blinding was not relevant to the study, as the performed experiments all produced quantitative data that were not open to interpretation by different researchers.

Reporting for specific materials, systems and methods

We require information from authors about some types of materials, experimental systems and methods used in many studies. Here, indicate whether each material, system or method listed is relevant to your study. If you are not sure if a list item applies to your research, read the appropriate section before selecting a response.

Materials & experimental systems

n/a	Involved in the study
<input type="checkbox"/>	<input checked="" type="checkbox"/> Antibodies
<input type="checkbox"/>	<input checked="" type="checkbox"/> Eukaryotic cell lines
<input checked="" type="checkbox"/>	<input type="checkbox"/> Palaeontology and archaeology
<input checked="" type="checkbox"/>	<input type="checkbox"/> Animals and other organisms
<input checked="" type="checkbox"/>	<input type="checkbox"/> Clinical data
<input checked="" type="checkbox"/>	<input type="checkbox"/> Dual use research of concern
<input checked="" type="checkbox"/>	<input type="checkbox"/> Plants

Methods

n/a	Involved in the study
<input checked="" type="checkbox"/>	<input type="checkbox"/> ChIP-seq
<input checked="" type="checkbox"/>	<input type="checkbox"/> Flow cytometry
<input checked="" type="checkbox"/>	<input type="checkbox"/> MRI-based neuroimaging

Antibodies

Antibodies used

Primary Antibodies (all used at 1:1000 dilution): anti-VSV-G [8G5F11], anti-VSV-N [10G4] (Kerafast); anti-V5 [D3H8Q] (Cell Signaling Technology); anti-GAPDH [14C10] (Cell Signaling Technology); HA [3F10] (Roche); FLAG [M2] (Sigma); HaloTag (Promega); human IFIT1 [3G8] (Novus Biologicals)

Secondary Antibodies (all used at 1:10000 dilution): Goat Anti-Rabbit IgG (H + L)-HRP Conjugate (Bio-Rad), Goat Anti-Mouse IgG (H + L)-HRP Conjugate (Bio-Rad), Goat anti-Rat IgG (H+L) Secondary Antibody, HRP (Invitrogen)

Validation

anti-VSV-G: from the Kerafast website - "BHK cells were infected with VSV and labeled with Anti-VSV-G (8G5F11) and JacksonLabs Dylight 549 goat anti-mouse secondary antibody. Cells were imaged at 20X using QImaging Camera (half of 14-bit range with < 1000 ms exposure). Cells were stained and imaged live. (contrast adjusted 8-bit image)." There are also 46 related publications listed.

Anti VSV-N: the Kerafast website lists 9 related publications.

Anti-V5: the Cell Signaling Technology website presents validation data from western blots, immunoprecipitation, microscopy, and flow cytometry. There are 464 related publications.

Anti-GAPDH: the Cell Signaling Technology website presents validation data from western blots, immunohistochemistry, microscopy, and flow cytometry. There are 8933 related publications.

Anti-HA: the Sigma website presents validation data from western blots. There are 41 related publications.

Anti-FLAG: the Sigma website presents validation data from microscopy, western blots, and ELISA. There are 9676 related publications.

Anti-HaloTag: the Promega website presents validation data from western blots. They do not list related publications.

Anti-Human IFIT1: the Novus website presents validation data from western blots, immunohistochemistry, microscopy, and flow cytometry. There is 1 related publication.

Goat Anti-Rabbit IgG (H + L)-HRP Conjugate, Goat Anti-Mouse IgG (H + L)-HRP Conjugate: Bio-Rad provides a PDF of supporting documentation that lists 1 related publication.

Goat anti-Rat IgG (H+L) Secondary Antibody, HRP (Invitrogen) : the Invitrogen website provides multiple figures, including blots, of supporting data for validation.

Eukaryotic cell lines

Policy information about [cell lines and Sex and Gender in Research](#)

Cell line source(s)

HEK293T, BHK-21, and H1HeLa cells were obtained from ATCC (catalog # CRL-3216; # CCL-10; # CRL-1958, respectively). Flp-In T-REx HEK293 cells were obtained from Thermo Fisher (Invitrogen, catalog # R78007). Inducible lines expressing mCherry, IFIT2, IFIT3, and IFIT2-IFIT3 were generated according to the manufacturer's protocol. MEFs from Ifit2-/- and ΔIfit3a/b mice were prepared from day 13.5-14.5 embryos according to published protocols (Tan Y.S. and Lei Y.L., 2019. Methods Mol Biol.). Because of the early stage of embryo development, mice could not be externally sexed; however, since gross decreases in litter size for the KO animals (8-10 pups per litter) were not observed, we assume that there was a mix of male and female embryos.

Authentication	HEK293 cells were authenticated by STR. Successful generation of inducible Flp-In lines were authenticated by induction with doxycycline followed by fluorescence imaging for mCherry or western blot for IFIT2 and/or IFIT3.
Mycoplasma contamination	All lines are regularly tested for Mycoplasma contamination, and cell lines used in this manuscript were Mycoplasma-free.
Commonly misidentified lines (See ICLAC register)	None of our cell lines appear on the list.

Plants

Seed stocks	<i>Report on the source of all seed stocks or other plant material used. If applicable, state the seed stock centre and catalogue number. If plant specimens were collected from the field, describe the collection location, date and sampling procedures.</i>
Novel plant genotypes	<i>Describe the methods by which all novel plant genotypes were produced. This includes those generated by transgenic approaches, gene editing, chemical/radiation-based mutagenesis and hybridization. For transgenic lines, describe the transformation method, the number of independent lines analyzed and the generation upon which experiments were performed. For gene-edited lines, describe the editor used, the endogenous sequence targeted for editing, the targeting guide RNA sequence (if applicable) and how the editor was applied.</i>
Authentication	<i>Describe any authentication procedures for each seed stock used or novel genotype generated. Describe any experiments used to assess the effect of a mutation and, where applicable, how potential secondary effects (e.g. second site T-DNA insertions, mosaicism, off-target gene editing) were examined.</i>